Gondwana Research 110 (2022) 283–304

Contents lists available at ScienceDirect

Gondwana Research

journal homepage: www.elsevier.com/locate/gr

Past, present and future global influence and technological applications of iron-bearing metastable nanominerals

Manuel A. Caraballo [a,b,c,d,*], Maria P. Asta [e,f], Jeffrey Paulo H. Perez [g,h], Michael F. Hochella Jr. [i,j]

[a] Department of Water, Mining and Environment, Scientific and Technological Center of Huelva, University of Huelva, 21004 Huelva, Spain
[b] Department of Mining, Mechanic, Energetic and Construction Engineering, Higher Technical School of Engineering, University of Huelva, Avda. de las Fuerzas Armadas, S/N, 21071 Huelva, Spain
[c] Mining Engineering Department, University of Chile, Avda. Tupper 2069, Santiago, Chile
[d] Advanced Mining Technology Center, University of Chile, Avda. Tupper 2007, 8370451 Santiago, Chile
[e] Institute of Earth Surface Dynamics, Faculty of Geosciences and Environment, University of Lausanne, 1015 Lausanne, Switzerland
[f] Department of Mineralogy and Petrology, University of Granada, Fuentenueva s/n, Granada 18071, Spain
[g] Sec. 3.5 Interface Geochemistry, GFZ German Research Centre for Geosciences, Telegrafenberg, 14473 Potsdam, Germany
[h] Department of Earth Sciences, Freie Universität Berlin, 12249 Berlin, Germany
[i] Department of Geosciences, Virginia Tech, Blacksburg, VA 24061, USA
[j] Earth Systems Science Division, Energy and Environment Directorate, Pacific Northwest National Laboratory, Richland, WA 99352, USA

ARTICLE INFO

Article history:
Received 29 September 2021
Revised 19 November 2021
Accepted 19 November 2021
Available online 1 December 2021

Keywords:
Ferrihydrite
Schwertmannite
Green rust
Nanotechnology
Nanogeosciences

ABSTRACT

Iron-bearing nanominerals such as ferrihydrite, schwertmannite, and green rust behave as metastable precursors leading to the formation of more thermodynamically stable iron mineral phases (e.g., jarosite, goethite, hematite, and magnetite). However, this transformation may last from days to tens or even hundreds of years, making them the most predominant iron-bearing minerals at environmental conditions and at the human time scale. The present review characterizes ferrihydrite, schwertmannite, and green rust nanominerals according to their main physical and chemical properties, and at both nano- and *meso*-scales. It also presents a comprehensive review of the multiple past and present Earth environments where these nanominerals have played, and still play, a pivotal role in the geochemistry, mineralogy and environmental nanogeosciences of these environments. Finally, the present and future technological applications of these nanominerals as well as their role in the generation of a more sustainable human-Earth relationship is discussed, with a special emphasis on their use in new circular economies and green based technologies.

1. Metastable iron-bearing nanominerals

Nanominerals are those minerals that only exist in the nanoparticle size range, often between ~1 nm up to a few to several tens of nm, or clays that only exist with at least one dimension in that size range (Hochella et al., 2008). Separate from this, mineral nanoparticles are those that refer to nanosized particles of minerals that typically develop into larger crystals (from μm to m). Both nanominerals and mineral nanoparticles display physical and chemical properties such as stability and reactivity that could significantly change as a function of their size and shape (Caraballo et al., 2015), and typically differ from the properties of their bulk scale counterparts (if any). In this regard, metastable environmental nanominerals (e.g., green rust, GR) and especially the ones exhibiting very poor atomic order (e.g., ferrihydrite, Fh, and schwertmannite, Schw) or amorphous structures (e.g., amorphous calcium carbonate, and amorphous silica) have been reported to display a wide range of physicochemical properties like solubility products, chemical compositions, and adsorption capacities, among others (Caraballo et al., 2013). This review focuses on

Abbreviations: GR, Green rust; Fh, Ferrihydrite; Schw, Schwertmannite; SRO, Short range order; MRO, Medium range order; LRO, Long range order; XTS, X-ray total scattering; HRTEM, High resolution transmission electron microscopy; EXAFS, Extended X-ray absorption fine structure; XANES, X-ray absorption near-edge structure; IMA, International Mineralogical Association; XRD, X-ray diffraction; STEM, Scanning transmission electron microscopy; PDF, Pair distribution function; EELS, Electron energy loss spectroscopy; IR, Infrared spectroscopy; DTA, Differential thermal analysis; ED, Electron diffraction; ND, Neutron diffraction; EA, Elemental analysis.

* Corresponding author.
E-mail address: mcaraballo@dimme.uhu.es (M.A. Caraballo).

https://doi.org/10.1016/j.gr.2021.11.009
1751-7311/

metastable environmental nanominerals within the Fe geochemical cycle. More specifically, the review involves the occurrence of three metastable nanominerals (i.e., Fh, Schw, and GR) that can be formed along very broad ranges of water pH conditions and redox environments (Fig. 1).

These three nanominerals are especially useful for showing the implications resulting from different grades of crystallinity including specific and special physicochemical properties. As shown in Fig. 1a, GR is typically characterized by a well-defined crystal structure with long range order predominantly in two spatial directions, whereas Fh and Schw are typically poorly or very poorly crystalline (i.e., exhibiting only medium- or short-range order) in all spatial directions. In addition, and as will be discussed in-depth during this review, these three nanominerals of metastable nanominerals have been reported as ubiquitous in surficial natural and anthropogenic environments. They are being intensely studied as possible nanomaterials for various environmental and technological applications.

For the sake of clarity, the iron metastable nanominerals formed in oxidizing environments (Fh and Schw) will be presented first, followed by the iron metastable nanomineral formed in reducing environments (GR).

1.1. Giving recognition to Fe metastable nanominerals

Iron metastable nanominerals do not fit the aspects of the long-standing formal definition of a mineral as a homogeneous substance with clearly defined chemical composition and crystalline structure (Hochella et al., 2008). However, despite the lack of consensus regarding their crystal structures, homogeneities, and even compositions, and regardless whether they are considered as very poorly ordered or even partially amorphous nanominerals, Fh, Schw and GR were first considered to be minerals a few to many decades ago (i.e., 1935, 1948, 1994; respectively). Notwithstanding these original assessments, scientific research on these nanominerals did not significantly increase until the last two or three decades (Fig. 2). This likely came about due to the improvement and better availability of state-of-the-art analytical techniques, mainly high-resolution transmission electron microscopy (HRTEM) coupled with electron spectroscopy and diffraction, and synchrotron-based techniques (e.g., X-ray total scattering, XTS; extended X-ray absorption fine structure, EXAFS; X-ray absorption near edge structure, XANES), needed to unambiguously identify and study these nanominerals (Caraballo et al., 2015).

As shown in Fig. 2, Fh is by far the most studied and reported iron-bearing nanomineral among the those covered in this review, followed by GR and finally Schw. Together, they account for more than 4,500 new publications just in the last decade.

Natural ferrihydrite (Fh) was first described on the walls of the old mine workings in the Altay deposits (Chukhrov et al., 1971). The diffraction patterns of this material (Chukhov et al., 1974; Chukhrov et al., 1972) were consistent with those obtained from a synthetic Fe (hydr)oxide precipitate obtained by forced hydrolysis of a ferric nitrate solution and for a Fe micelle extracted from ferritin, a biological Fe storage protein (Towe and Bradley, 1967). The name ferrihydrite was proposed by Chukhov et al. (1974) and Chukhrov et al. (1973), and both the mineral and name were approved shortly thereafter by the International Mineralogical Association (IMA) (Fleischer et al., 1975). Now, the ubiquity of ferrihydrite as a naturally occurring nanomineral is well-recognized and presently it is found globally in surface aerated environments (see also Section 2.2 below).

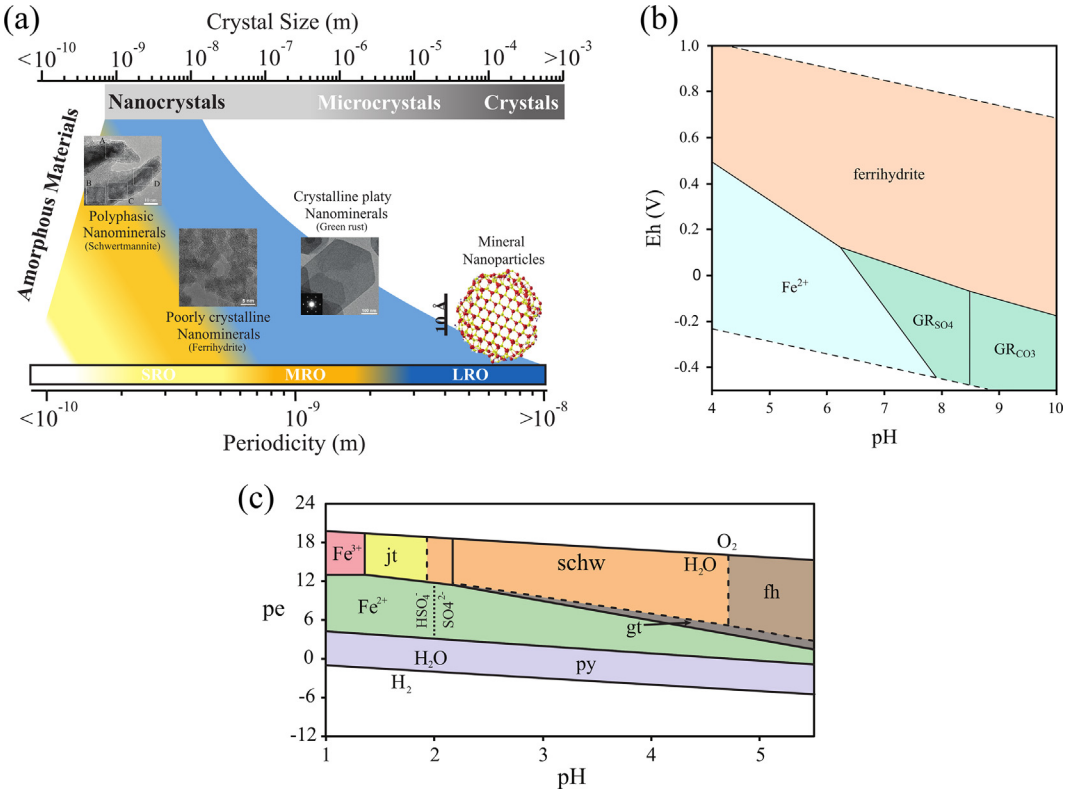

Fig. 1. (a) Schematic diagram organizing iron-bearing nanominerals (i.e., schwertmannite, ferrihydrite, green rust) and mineral nanoparticles according to their range order (SRO, MRO and LRO stands for Short-, Medium, and Long Range Order; modified from Caraballo et al. 2013). Pourbaix diagrams showing the main predominance fields for the (b) metastable phases in a suboxic groundwater (modified from Perez et al., 2020) and (c) Fe–S–K–O–H system at 298 K and 1 bar (modified from Caraballo et al., 2013). (For interpretation of the references to colour in this figure legend, the reader is referred to the web version of this article.)

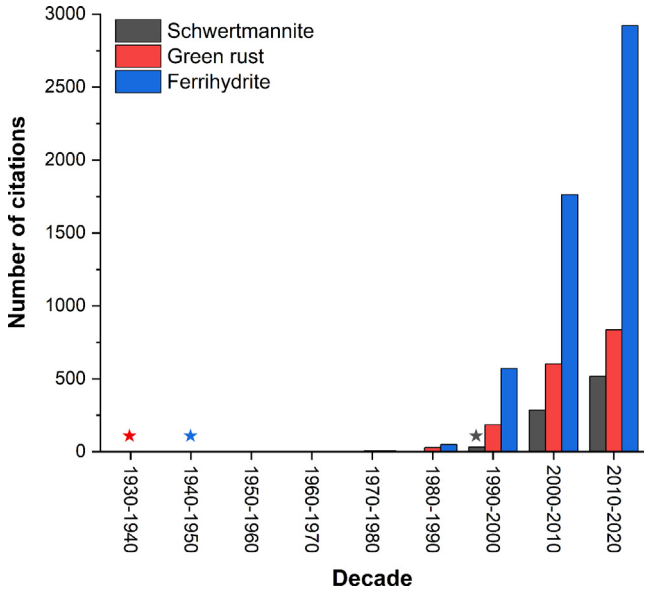

Fig. 2. Number of new publications by decade for the three nanominerals under study. Colored stars mark each nanomineral first report. Based on three different searches on Web of Science (09–14-2021) using the following searching criteria: TITLE-ABS-KEY: "*mineral name*". *Mineral name*: ferrihydrite or green rust or schwertmannite. (For interpretation of the references to colour in this figure legend, the reader is referred to the web version of this article.)

Schwertmannite (Schw) is an abundant, poorly crystalline ferric oxyhydroxysulfate mineral that primarily precipitates in acidic sulfate environments (Section 2.2). Early studies described it as an ochreous ferrihydrite-like precipitate isolated from a stream receiving acid-sulfate mine drainage (Brady et al., 1986) and also as a mineral synthesized in the laboratory by bacterially-induced oxidation of an $FeSO_4$ solution at pH 2.5 (Murad, 1988). Several years later, Bigham et al. (1990) described and identified a poorly crystallized oxyhydroxysulfate of iron formed by bacterial oxidation of Fe(II) in acid mine effluents in the eastern Ohio coalfield and from drainage exiting an abandoned copper-arsenic mine in Finland. Its atomic structure was thought to be similar to a tunnel structure akin to that of akaganeite. This poorly crystallized oxyhydroxysulfate of iron was approved as a mineral by the IMA in 1990. Two years later in 1992, the Commission on New Minerals and Mineral Names accepted the name "schwertmannite", in honor of professor Udo Schwertmann, for this ferric oxyhydroxide sulfate with the ideal formula between $Fe_8O_8(OH)_6SO_4$ and $Fe_{16}O_{16}(OH)_{10}(SO_4)_3$ (Bigham et al., 1996, 1994, 1990). Bigham et al. (1994) also suggested the presence of Schw as a new oxyhydroxysulfate of iron in the Pyhäsalmi sulphide mine, Province of Oulu, Finland and Schwertmann et al. (1995) reported the first fully natural occurrence of Schw in a small stream draining a pyritic schist at the Pfitscher Joch (Zillertaler Alps, Austria). Since then, the presence of Schw has been reported in almost every country in the world reporting the existence of natural or anthropogenic acid sulfate waters (e.g., Acero et al., 2006; Asta et al., 2010a, 2010b; Burton et al., 2007; Fitzpatrick et al., 2012; Fukushi et al., 2003; Kawano and Tomita, 2001; Regenspurg et al., 2004).

GR phases are mixed-valence Fe layered hydroxide that were originally studied as metastable intermediates during the corrosion of steel (and other ferroalloys) under near-neutral to alkaline conditions (Girard & Chaudron, 1935; McGill et al., 1976; Stampfl, 1969). They are typically found in between the upper layer of the corrosion products and the metallic iron substrate (Takahashi et al., 2005; Suzuki et al., 2007). The first synthetic GRs were first reported in 1950, and were synthesized in the laboratory either by titration of a mixed Fe^{2+} and Fe^{3+} solution with NaOH until near-neutral pH (Arden, 1950), or oxidation of ferrous hydroxide (white rust; $Fe(OH)_2$) precipitate (Feitknecht and Keller, 1950).

Although first observed as a corrosion product, their presence in natural environments have long been suggested by the bluish-green shade of poorly drained (i.e., hydromorphic/gley) soils which turn ochre upon exposure to air (Taylor, 1980). In 1997, Trolard et al. (1997) identified a naturally occurring GR belonging to the hydrotalcite group, for the first time, in a gley soil in forest of Fougères in Brittany, France using ^{57}Fe Mössbauer spectroscopy and microprobe Raman spectroscopy. GR was finally recognized as a mineral in 2003 with the name fougerite (IMA 2003-057), based on the forest of Fougères in Brittany where it was first identified (Trolard et al., 2007).

1.2. Crystal structure and main physical and chemical properties

Having the correct structural model of an amorphous, nearly amorphous, or polyphasic solid, as in the case of crystalline materials, is crucial in understanding its physical–chemical characteristics and behavior in both natural and materials science settings. A reliable structural model is essential to predict the thermodynamic and magnetic properties (Guyodo et al., 2006; Majzlan et al., 2004; Navrotsky et al., 2008), as well as the solid surface and chemical reactivity, which plays a key role in the sorption and release of pollutants (Burton et al., 2009; Lozano et al., 2020; Marouane et al., 2021; Waychunas et al., 1993). However, the determination of the structure of natural nanominerals is often times problematic due to their small sizes, disordered structure, and structural variability exhibited under different environments (Caraballo et al., 2015). In bulk crystalline materials, sharp Bragg reflections that arising from lattice periodicity (i.e., long-range order; LRO) contain enough information to solve the structure. However, due to the absence of these Bragg spots or reflections in amorphous materials, the characterization of their structures has been challenging for the scientific community. This is mainly caused by the limitation of traditional 'Bragg scattering' techniques to elucidate the nanostructure of mineral nanoparticles (Caraballo et al., 2015; Sestu et al., 2017). However, the refinement and development of a wide array of nanoscale techniques (e.g., HRTEM), synchrotron-based methods (e.g., XTS, EXAFS and/or XANES spectroscopies) and computational methods (e.g., ab initio calculations, Monte Carlo simulations, pair distribution functions, etc.) have allowed for a description of the structural ordering over short- and medium-range length scales and obtaining a better characterization of nanominerals (Caraballo et al., 2015; Maurice and Hochella, 2008; Trejos et al., 2021; Schneider et al., 2020; Lima et al., 2021; Oliveira et al., 2021a).

1.2.1. Ferrihydrite

The structure of Fh has been the subject of debate and the object of numerous studies over the past 50 years (Eggleton and Fitzpatrick, 1988; Gilbert et al., 2013; Harrington et al., 2011; Hiemstra, 2013; Janney et al., 2001, 2000; Maillot et al., 2011; Manceau, 2011, 2009; Michel et al., 2007; Rancourt and Meunier, 2008; Towe and Bradley, 1967; Zhao et al., 1994). Despite the valuable information provided by those studies, an unequivocal description of the atomic structure and composition of Fh have not been yet accepted (Sassi and Rosso, 2019a). Key aspects of this problem reside in the combination of a very small particle size giving rise to severe powder diffraction peak broadening, a high degree of defect incorporation (Funnell et al., 2020), and to its compositional variability sensitive to the conditions of formation such as temperature, pH, aging time, etc. (Sassi and Rosso, 2019a). From all the structural models proposed over the years (see Table 1 and reviews from Bowles, 2021; Jambor and Dutrizac, 1998; and Singh

Table 1
Main studies proposing a Fh crystal structure. Modified from Chappell et al. 2017.

Study	Techniques Used	Sample type	Implications
Towe and Bradley, 1967	IR; XRD; DTA	Ferritin; 2L-Fh, prepared at 85 °C. Samples dried at 50 °C and 110 °C	Hematite-like structure; Oct and Tet Fe sites
Harrison et al., 1967	XRD and ED	Ferritin	Oct and Tet Fe sites
Heald et al., 1979	XAFS	Ferritin	Oct and Tet Fe sites
Eggleton and Fitzpatrick, 1988	XANES; ED; XRD, DTA	2L-Fh and 6L-Fh. Prepared at 60 °C and 75 °C, respectively	Oct and Tet (36%) Fe sites; development of maghemite after 300 ∘C
Drits et al., 1993	XRD	2L-Fh and 6L-Fh	Three-component model; defective, defect-free and ultradispersed hematite (10%). Oct Fe only sites
Zhao et al., 1994	XAFS	2L-Fh and 6L-Fh. Prepared at various temperatures between 50 °C and 500 °C	Oct and Tet (10%) Fe sites. Tet sites at the surface
Manceau and Gates, 1997	XANES	2L-Fh and 6L-Fh prepared at 92 °C and air-dried at 25 °C	Oct Fe sites. Over estimation of Tet Fe sites, from previous study
Jansen et al., 2002	XRD, ND	6L-Fh Prepared at 75 °C	No hematite. 50% defective, 50% defect-free phases
Michel et al., 2007	XRD, PDF	2L-Fh prepared at 23 °C, 3L-Fh, 6L-Fh prepared at 75 °C	Single-phase model with both Oct and Tet (20%) Fe sites
Rancourt and Meunier, 2008	XRD	2L-Fh prepared at 60 ∘Cand dried at 110 °C. 6L-Fh prepared at 75 °C	Single-phase structure incorrect
Malliot et al., 2011	XAFS	2L-Fh prepared at 75 °C, air-dried. 4L-Fh, 5L-Fh, and 6L-Fh	Oct and Tet (15%-35%) Fe sites
Vaughan et al., 2012	EELS	2L-Fh and 6L-Fh. Prepared at 70 °C	Oct and Tet (10%) Fe sites
Chappell et al., 2017	ND, PDF, XRD, EA	2L-Fh, prepared at 20 °C, dried at 40 °C	Single-phase model resolved
Funnell et al., 2020	PDF, RM	2L-Fh	Single-phase model gave the best fit

IR: Infrared spectroscopy; XRD: X-ray Diffraction; DTA: differential thermal analysis; ED: electron diffraction; ND: neutron diffraction, EXAFS: X-ray absorption fine structure; XANES: X-ray absorption near edge structure.
PDF: pair distribution function; EELS: electron energy loss spectroscopy; EA: elemental analysis.

et al., 2010), there are mainly two competing models that are still debated within the community: (i) a multi-phase model (Drits et al., 1993) and (ii) a single-phase model (Michel et al., 2010, 2007) (Fig. 3).

The multi-phase model, based on X-ray diffraction (XRD) patterns and EXAFS spectroscopy (Manceau and Drits, 1993), proposes that ferrihydrite has a trigonal structure (space group *P*31*c*) composed of three different phases: (i) a major defective, randomly occupied phase; (ii) a minor defect-free close packing phase and (iii) low levels of ultradispersed hematite. The defect-free phase shows an *ABACA* oxygen packing sequence wherein Fe atoms occupy 50% of the available octahedral sites, having the anionic packing with unit cell parameters (a = 2.96 Å and c = 9.4 Å) similar to the ones proposed by Harrison et al. (1967). The defective ferrihydrite structure consists of randomly sequenced *ABA* and *ACA* structural fragments. The defect-free phase is similar to feroxyhite (δ-FeOOH). The third component is an ultradispersed phase, which is a combination of subordinate amounts of nanocrystalline phases, including hematite (α-Fe_2O_3) and a spinel-type phase (maghemite, γ-Fe_2O_3 or magnetite, Fe_3O_4), and highly-defective material. This model was supported by EXAFS and XANES results of Manceau and Gates (1997) examining the surface structure of ferrihydrite, which show that the octahedral-only three-phase model provides a match with their experimental data. Furthermore, this model has been confirmed by neutron and X-ray Rietveld refinement, electron nanodiffraction, and high angle annular dark field scanning transmission electron microscopy (HAADF-STEM) imaging (Janney et al., 2000; Jansen et al., 2002; Manceau, 2019). It is noteworthy that Jansen et al. (2002) suggested that the ultradispersed hematite was not required to obtain a good fit to the neutron diffraction pattern for six-line Fh. However, these results contrast with those of other studies based on EXAFS, XANES and electron energy loss spectroscopy (EELS) techniques (Eggleton and Fitzpatrick, 1988; Heald et al., 1979; Vaughan et al., 2012), which showed that ferrihydrite contains both octahedral and tetrahedral iron sites, although there is disagreement over the percentage of tetrahedral Fe.

On the other hand, Michel et al. (2010, 2007) proposed a single-phase model by analyzing the pair distribution function (PDF) derived from direct Fourier transformation of total X-ray scattering. This model structure, based upon isostructural akdalaite ($Al_{10}O_{14}(OH)_2$, space group $P6_3mc$), consists of 20% of the iron atoms involved in tetrahedral coordination and the remaining 80% in the typical octahedral coordination. This mix of octahedral and tetrahedral iron sites agrees with other reported models (Eggleton and Fitzpatrick, 1988; Harrington et al., 2011; Heald et al., 1979; Maillot et al., 2013; Vaughan et al., 2012; Zhao et al., 1994). Very recently, experimental and theoretical studies also support the Michel structure model (Chappell et al., 2017; Funnell et al., 2020; Sassi and Rosso, 2019a). However, this model has received criticisms related to the tetrahedral Fe-O bonds, inconsistencies with XRD patterns, and the anomalously H-poor formula ($Fe_{10}O_{14}(OH)_2$) compared to other measurements of ferrihydrite (Manceau, 2011, 2009; Manceau et al., 2014; Rancourt and Meunier, 2008).

Diffraction and pair distribution function (PDF) measurements have proven insufficiently discriminating to rule out either the multi-phase or single-phase model in any definitive sense (Funnell et al., 2020), because although they individually show in general an agreement with XRD and PDF, respectively, neither agree fully with both measurements simultaneously (Sassi and Rosso, 2019a). The difficulty in all comparative studies is that the Drits model requires significant simplifications (Manceau et al., 2014) to allow its complex composition to be approximated by a single damped periodic structure (Funnell et al., 2020). Recently, Sassi and Rosso (2019b) suggested that different structures for the core of ferrihydrite could simultaneously coexist. While the Michel model could be representative of a “dry” phase of ferrihydrite, the Drits model could well represent a “wet” phase counterpart.

The chemical composition of Fh have remained uncertain for a long time because the variability observed in the amounts of OH and H_2O relative to Fe (Fleischer et al., 1975; Russell, 1979; Stanjek and Weidler, 1992; Towe and Bradley, 1967; Xu et al.,

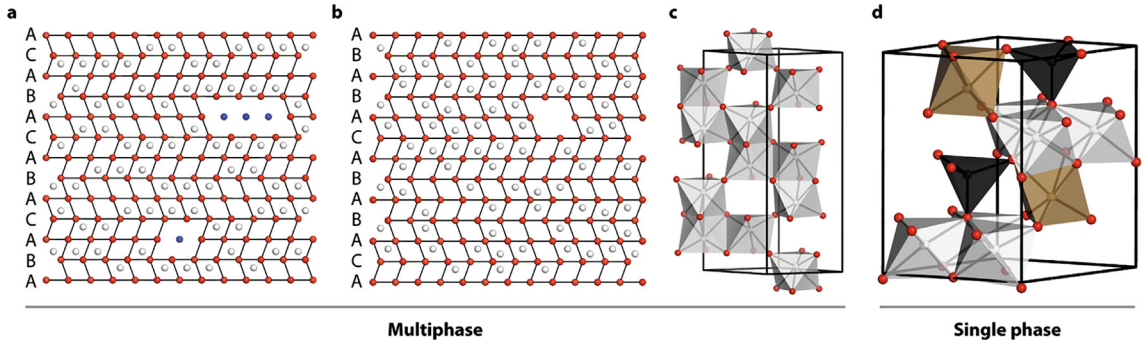

Fig. 3. **a** Representative slices of non-defective and b defective particles in the multiphase (MP) model of Fh, viewed along the⟨1 1 0⟩direction. White spheres represent Fe atoms, red, O atoms, and blue, water molecules. O anion vacancies can occur in defective particles where all neighboring Fe atoms are randomly vacant—inclusion of oxygen would be equivalent to the presence of water. c Hematite structure, which forms a third, minority, component of the MP model. d Single-phase (SP) model, where Fe1, Fe2 and Fe3 sites are shown as light grey, brown and black polyhedra, respectively. Reproduced with permission from Funnell et al. (2020). Copyright © Nature Publishing Group. (For interpretation of the references to colour in this figure legend, the reader is referred to the web version of this article.)

2011). The problem arises from the difficulty of separating structural hydroxyl and water from physically sorbed water, and therefore, many chemical formulas for ferrihydrite have been proposed (Table 2).

Considering all of them, the most widely accepted Fh formula is the initially suggested formula $Fe_5HO_8{\cdot}4H_2O$ (Chukhrov et al., 1972; Towe and Bradley, 1967). The same heterogeneity and discrepancies have been reported regarding the numerous solubility products proposed for 2-line and 6-line Fh (Table 3).

Most of the estimates for equilibrium constants have been reported for the following reactions:

(1) $Fe(OH)_3 + 3H^+ = Fe^{3+} + H_2O$ ($K_1 = a_{Fe3+} \cdot a_{H+}^{-3}$)
(2) $Fe(OH)_3 = Fe^{3+} + 3OH^-$ ($K_2 = a_{Fe3+} \cdot a_{OH-}^{3}$)

The significant discrepancies (up to three orders of magnitude and moving from negative to positive values) observed among the reported solubilities (Table 3) have been attributed to the low crystallinity, variable chemical composition and metastability of ferrihydrite with respect to other iron phases (e.g., goethite), and differences in age and particle size (Yu et al., 2002). Other reasons pointed out for the uncertainty in the solubility product values include the absence of hydrolysis species in the calculations (i.e., equilibrium may not have reached), or that the purity and composition of ferrihydrite may have not been checked (Cornell and Schwertmann, 2003).

1.2.2. Schwertmannite

Regarding Schw, the first model describing the structure of a "poorly crystalline sulfate oxyhydroxide" was proposed by Bigham et al. (1990). These authors synthesized akaganeite-like minerals with varying concentrations of sulfate. Based on the similarities of the XRD patterns obtained with the 8-diffraction lines characteristic of Schw, they suggested an akaganeite-like structure with the sulfate groups replacing the chlorides. Although other structures have been proposed, for example, a Fh-like structure (Loan et al., 2004), there is a general agreement that the schwertmannite structure consists of double chains of edge-sharing FeO_6 octahedra that form 2 × 2 channels where sulfate ions are located (Barham et al., 1997; Bigham et al., 1990; Fernandez-Martinez et al., 2010; Waychunas et al., 1995). This model was supported by the results of Fernandez-Martinez et al. (2010) based on PDF, XRD, and density functional theory (DFT) calculations. These authors suggested a deformed frame of iron octahedral similar to akaganeite, in which two sulfate molecules per unit cell form an outer-sphere and an inner-sphere complex inside the iron octahedral channels, which was also proposed by Boily et al. (2010), and later confirmed later by Sestu et al. (2017) using Reverse Monte Carlo/Debye Scattering Equation (RMC/DSE) refinements combined with S K-edge XANES information. The Schw structure refinement proposed by Sestu et al. (2017) is shown in Fig. 4.

An important result of this study is the unequivocal presence of goethite in Schw samples, usually hidden in the diffuse scattering of the diffraction pattern due to its difficult detection with conventional techniques. In addition, these authors also suggested that this could explain the wide range of values for the solubility

Table 2
Most frequent chemical formulas proposed for Fh.

Formula	Reference
$Fe_5\ HO_8{\cdot}4H_2O$	Towe and Bradley (1967), Chukhrov et al. (1972)
$5Fe_2O_3{\cdot}9H_2O$	Chukhrov et al. (1972)
$Fe_6(O_4H_3)_3$	Chukhrov et al. (1973)
$Fe_2O_3{\cdot}2FeOOH{\cdot}2.6H_2O$	Russell (1979)
$Fe(OH)_3$	Jambor and Dutrizac (1998), Majzlan et al. (2004), Navrotsky et al. (2008)
$Fe_2O_3{\cdot}9H_2O$	Chukhrov et al. (1972)
$Fe_2O_3{\cdot}3H_2O$ or $\cdot 2H_2O$	Eggleton and Fitzpatrick (1988)
$Fe_{4.5}(O,OH,H_2O)_{12}$	Generalization of the two formulas given by Eggleton and Fitzpatrick (1988)
FeOOH	Manceau et al. (2014)
Fe_5O_8H	Michel et al. (2010, 2007)

Table 3
Solubility products for ferrihydrite.

Equilibrium constants	Reference
$\log K_1 = 4.891$	Truesdell and Jones (1974)
$\log K_1 = 3.0$ to 5.0	Nordstrom et al. (1990)
$\log K_1 = 3.96 \pm 0.1$	Biedermann and Schindler (1957)
$\log K_1 = 3.55 \pm 0.1$	Schindler et al. (1963)
$\log K_2 = -37.3$	Langmuir and Whittemore (1971)
$\log K_2 = -39$	Norvell and Lindsay (1982)
$\log K_2 = -31.7$	Fox (1988)[1]
$\log K_1 = 4.3 \pm 0.25$	Yu et al. (1999)[2]
$\log K_1 = 4.23 \pm 0.70$	Yu et al. (2002)[3]
$\log K_1 = 5.06 \pm 0.35$	Yu et al. (2002)[2]
$\log K_1$ = 3.4 ± 0.5 – 4.0 ± 0.5	Majzlan et al. (2004)[3]
$\log K_1$ = 3.0 ± 0.5 – 3.4 ± 0.5	Majzlan et al. (2004)[2]
$\log K_2 = -39.5 \pm 0.1$	Baes and Mesmer (1976)
$\log K_2 = -38.6 \pm 0.2$	Stefánsson (2007)
$\log K_2 = -38.5 \pm 0.1$	Hiemstra (2015)[3]
$\log K_2 = -39.5 \pm 0.1$	Hiemstra (2015)[2]

[1] Constant calculated as $a_{Fe3+} \cdot a_{OH}^{2.35}$.
[2] Value proposed for 6-line ferrihydrite.
[3] Value proposed for 2-line ferrihydrite.

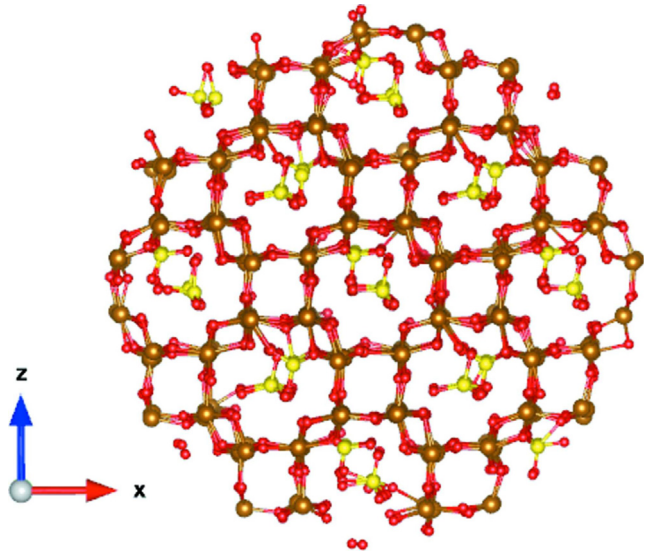

Fig. 4. Three-dimensional particle model for Schw obtained after the RMC refinement of the Bigham model. Red spheres are O atoms, brown spheres are Fe atoms and yellow spheres are S atoms (Sestu et al., 2017). Reproduced with permission of International Union of Crystallography, according to the terms and conditions of use of material published by the International Union of Crystallography. (For interpretation of the references to colour in this figure legend, the reader is referred to the web version of this article.)

product reported in the literature (e.g., Caraballo et al., 2013). In the same line of reasoning, the concept of polyphasic nanominerals was coined, in the HRTEM study performed by French et al., (2012), to name the coexistence of nanodomains with goethite crystal structure and amorphous nanodomains forming Schw.

Similar to Fh, the chemical formula of Schw has also been the object of controversy and wide discrepancies. The first chemical formula, $Fe_8O_8(OH)_{8-x}(SO4)_x$ with x varying from 1 to 1.75, was proposed by Bigham et al. (1994). Later, Yu et al. (1999) estimated that x varies from 1.74 to 1.86. In an attempt to settle these discrepancies, Caraballo et al., (2013) used data from 30 different pure Schw samples from around the world and reported an even wider range for ×, spanning from 0.75 to 2.58. This uncertainty on Schw compositional range could be explained by the different location of the sulfate groups in the structure (Fernandez-Martinez et al., 2010). As it was shown for Fh, this wide range of Schw bulk chemistries and the very different environmental conditions where it can be formed (e.g., water pH, temperature, elemental concentrations, presence of bacteria, etc.) induce the existence of a corresponding wide range of solubility constants (Caraballo et al., 2013 and references therein). In this regard, Caraballo et al. (2013) obtained a range for the logarithm of the solubility product (K_{sp}) of 30 natural samples between 5.8 and 39.5. Nevertheless, the most commonly accepted and used values for the log K_{sp} are still 7.06 ± 0.09 (Kawano and Tomita, 2001), 10.05 ± 2.5 (Yu et al., 1999) and 18.0 ± 2.5 (Bigham et al., 1996).

1.2.3. Green rust

On the other hand, GR belongs to the hydrotalcite supergroup of LDHs, and is therefore composed of positively charged brucite-like layers of octahedrally coordinated Fe(II)-Fe(III) hydroxides that alternate with negatively charged interlayers of anions and water molecules (Fig. 5; Usman et al., 2018).

These brucite-like layers and interlayer regions are held together by hydrogen bonding and electrostatic forces. GR is usually represented by the general formula, $[Fe^{II}_{(1-x)}Fe^{III}_x(OH)_2]^{x+}[(x/n)A^{n-}{\cdot}mH_2O]^{x-}$, where A^{n-} is the intercalated anion, x is the molar fraction of Fe^{III}, $[Fe^{III}]/[Fe_{total}]$. Although there is no established nomenclature for naming different phases, GR is usually named based on the anionic species present in the interlayer: GR_z where z is the interlayer anion. An overview of common GR phases is shown in Table 4.

The molar fraction (x) of Fe(III) in the GR structure typically ranges from 0.25 to 0.33 (Murad and Taylor, 1984). The upper limit of $x \approx 0.33$ ensures a long-range order of Fe(II) cations surrounded by six Fe(II) cations in hexagonal arrangement (Génin et al., 2005). Moreover, GRs with $x > 0.33$ are *quasi*-absent due to strong electrostatic cation-cation repulsion in the crystal structure as a result of the high density of Fe(III) octahedral in the hydroxide layer. This leads to a disordered Fe hydroxide structural lattice and can act as nuclei for the formation of additional mixed-valent iron solid phases such as magnetite (Fe_3O_4) (Génin et al., 2005; Newman and Jones, 1998; Ruby et al., 2003).

The nature of the intercalated anions between the Fe(II)-Fe(III) hydroxide layers influences the structure and composition of GR. Depending on the intercalated anion, GR can be classified into two major groups: green rust one (GR1) and green rust two (GR2) (Bernal et al., 1959). GR1s have spherical or planar anions (e.g., Cl^-, CO_3^{2-}) while GR2s have tetrahedral anions (e.g., SO_4^{2-}, SeO_4^{2-}) intercalated in their respective layered structure. The difference in the molecular geometry of the corresponding intercalated anion in GR results in different characteristic stacking arrangements of the Fe(II)-Fe(III) hydroxide layers along the c-axis, and in turn their corresponding basal spacing (d_0). The crystal structure of GR1 is isomorphous to pyroaurite ($Mg^{II}_6Fe^{III}_2(OH)_{16}CO_3{\cdot}4H_2O$) or hydrotalcite ($Mg^{II}_4Fe^{II}_2(OH)_{12}CO_3{\cdot}3H_2O$). Hence, GR_{Cl} ($d_0 \approx 7.6$ Å) and

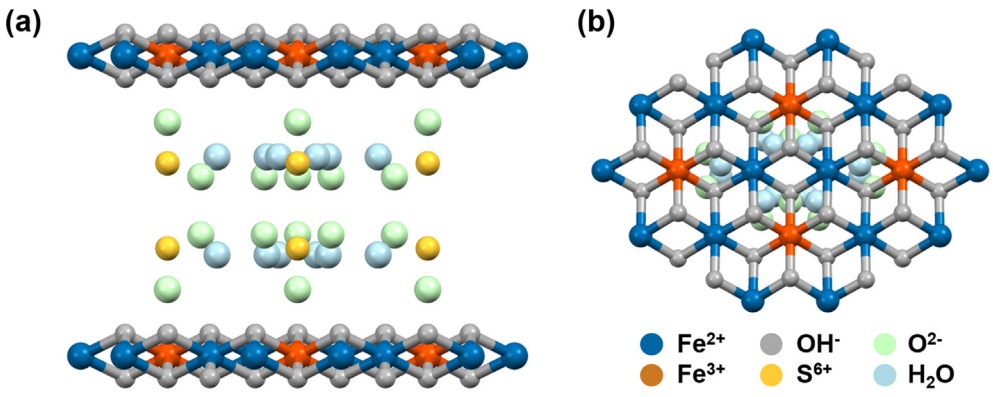

Fig. 5. (a) Crystal structure of GR_{SO4} along the [001] zone axis showing the Fe(II)-Fe(III) brucite-like layers and the interlayer region containing a double sheet of hydrated SO_4^{2-} ions. (b) Projection of the GR_{SO4} structure on the (001) plane illustrating the hexagonal octahedrally coordinated Fe(II) and Fe(III) hydroxides. Crystal structure was drawn using Mercury software (Macrae et al., 2008) based on the crystallographic information from Simon et al. (2003).

Table 4
Overview of known natural and synthetic GR phases based on the interlayer anion.

Anion	Chemical formula	Space group	Cell parameters		Basal spacing (Å)	Synthesis route	Reference
			a (Å)	*c* (Å)			
Inorganic							
Br^-	–	R3m	3.18	22.8	–	Oxidation	Bernal et al., 1959
Cl^-	$Fe^{II}_3Fe^{III}(OH)_8Cl{\cdot}mH_2O$	R3m	3.19	23.9	7.95	Oxidation	Refait et al., 1998a
ClO_4^-	$Fe^{II}_3Fe^{III}_2(OH)_{10}(ClO_4)_2{\cdot}mH_2O$	–	–	–	–	Oxidation	Vinš et al., 1987
CO_3^{2-}	$Fe^{II}_4Fe^{III}_2(OH)_{12}CO_3{\cdot}3H_2O$	R3m	3.18	22.7	7.57	Coprecipitation	Aissa et al., 2006
			3.16	22.5	–	Oxidation	Drissi et al., 1995
			3.16	22.5	–	Electrochemical deposition	Legrand et al., 2001
F^-	$Fe^{II}_3Fe^{III}(OH)_8F{\cdot}mH_2O$	–	–	–	–	Oxidation	Choi and Batchelor, 2008
I^-	–	–	3.19	24.8	–	Oxidation	Vinš et al., 1987
OH^-	$(Fe^{II},Mg)_6Fe^{III}_2(OH)_{18}{\cdot}4H_2O$ (fougerite)	R3m	3.13	22.7–23.9		Naturally occuring	Trolard et al., 2007
SeO_4^{2-}	$Fe^{II}_4Fe^{III}_2(OH)_{12}SeO_4{\cdot}8H_2O$	P3m1	–	–		Oxidation	Refait et al., 2000
SO_3^{2-}	$Fe^{II}_6Fe^{III}_2(OH)_{16}SO_3{\cdot}mH_2O$	R3m	3.22	23.4		Oxidation	Simon et al., 1998
SO_4^{2-}	$Fe^{II}_4Fe^{III}_2(OH)_{12}SO_4{\cdot}8H_2O$	P3m1	5.52	11	11	Oxidation	Simon et al., 2003
			3.18	10.9	10.9	Coprecipitation	Géhin et al., 2002
SO_4^{2-} (Na)	$NaFe^{II}_6Fe^{III}_3(OH)_{18}(SO_4)_2{\cdot}12H_2O$	P3	9.53	11	11	Oxidation	Christiansen et al., 2009b
Organic							
Benzene sulfonate	$Fe^{II}_4Fe^{III}_2(OH)_{12}(C_6H_6SO_3)_{0.2}(SO_4)_{0.8}{\cdot}mH_2O$	–	–	–	14.3	Ion exchange	Perez et al., 2018
Formate	$Fe^{II}_5Fe^{III}_2(OH)_{14}(CHO_2)_2{\cdot}3H_2O$	R3m	–	–	–	Oxidation	Genin and Ruby, 2008; Refait et al., 2007
Lactate	$Fe^{II}_3Fe^{III}(OH)_{16}C_3H_5O_3{\cdot}mH_2O$	R3m	3.18	44.1	14.8	Oxidation	Sabot et al., 2007
LAC[a]	–	–	–	–	28.3–44.4	Ion exchange	Ayala-Luis et al., 2010a
	$Fe^{II}_3Fe^{III}(OH)_5(C_{12}H_{23}O_2)_{0.7}(SO_4)_{0.5}{\cdot}mH_2O$ (dodecanoate, C12)	–	–	–	33	Coprecipitation	Huang et al. 2013
	–	–	–	–	26.8–41.6	Coprecipitation	Ayala-Luis et al., 2010b
LAS[b]	–	–	–	–	26.8–28.9	Ion exchange	Ayala-Luis et al., 2007
Oxalate	$Fe^{II}_6Fe^{III}_2(OH)_{16}C_2O_4{\cdot}3H_2O$	R3m	3.2	23.4	7.84	Oxidation	Refait et al., 1998b

GR_{CO3} ($d_0 \approx 7.6$ Å) both have rhombohedral lattice belonging to the $R\bar{3}m$ space group with a stacking sequence of *AcBiBaCjCbA*... where *A*, *B* and *C* are OH^- hexagonal layers, *a*, *b* and *c* are Fe cation layers and *i*, *j* and *k* are interlayer anions (Aissa et al., 2006; Génin and Ruby, 2004; Refait et al., 1998a). This stacking arrangement induces a three-layer repeat with a single plane of hydrated anions. On the other hand, GR_{SO4} ($d_0 \approx 11.0$ Å), which belongs to GR2, has a hexagonal lattice with a $P\bar{3}m1$ space group and a stacking sequence of *AcBij*..., which has a single-layer repeat with two planes of hydrated anions (Génin and Ruby, 2004; Simon et al., 2003).

Christiansen et al. (2009b) argued for the possibility of incorporating monovalent cations in the GR interlayer. The group proposed a sodium (Na) cation in the interlayer of the GR_{SO4} structure, with a chemical formula of ($NaFe^{II}_6Fe^{III}_3(SO_4)_2(OH)_{18}{\cdot}12H_2O$), as well as a different orientation of SO_4^{2-} in the interlayer space compared to the earlier proposed structure from Simon et al. (2003). Its crystal structure is similar to that of nikischerite ($NaFe^{II}_6Al_3(SO_4)_2(OH)_{18}{\cdot}12H_2O$) with a hexagonal lattice belonging to the $P\bar{3}$ space group (Huminicki and Hawthorne, 2003). They have also shown that other monovalent cations such as K^+, Rb^+ and Cs^+ can also be incorporated in the interlayer of GR_{SO4} with varying degrees of occupation based on the SO_4^{2-} pair stability constant (Christiansen et al., 2014).

The intercalated species in the GR structure are not limited to inorganic molecules. Using the same chemical design principle used in LDHs, a subclass of GR called organo-GRs, which have organic molecules in the interlayers, has also been prepared extensively over the past years. Various organic aliphatic and aromatic compounds such as low molecular weight organic acids, linear carboxylates and sulfonates (Table 4) have been used for synthesis up to now (Ayala-Luis et al., 2007; Ayala-Luis et al., 2010a,b; Génin and Ruby, 2008; Huang et al., 2013; Perez et al., 2018; Refait et al., 2007; Refait et al., 1998b; Sabot et al., 2007). In addition, and in the same line to the behavior shown by Schw and discussed in Section 1.2.2, Johnson et al., (2015) observed that naturally occurring GR nanoparticles and their synthetic analogues can be complex polycrystalline phases composed of crystallites only a few nanometers in size, and they often include nanometer-sized regions of amorphous material".

As it can be inferred from this section, as the crystallinity of the metastable iron-bearing nanominerals decreases, the disorder of the crystal structure increases, resulting in higher variability in their bulk chemistry and solubility products. This makes it difficult to realistically predict the precipitation or dissolution of these iron-bearing nanominerals using traditional hydrogeochemical models, where equations typically require the use of a single solubility product for a specific chemical reaction including a single bulk chemistry of the nanomineral. The generation of theoretical values (using the nanomineral modeled crystal structure) of their physicochemical properties (e.g., sorption capacity, specific weight, hardness) also becomes extremely challenging or even virtually impossible, resulting in the need to rely on the experimental measurements of their physicochemical parameters which may be quite heterogeneous and discrepant.

1.3. Iron-bearing nanominerals transformation to more stable minerals

1.3.1. Ferrihydrite

Fh is thermodynamically metastable (due to its poorly ordered structure and small particle size) and transforms to more stable phases such as goethite, hematite, lepidocrocite and magnetite (Boland et al., 2014; Li et al., 2020; Liu et al., 2010; Schwertmann et al., 2004; Schwertmann and Murad, 1983, see Fig. 6). The rate and extent of this transformation is affected by different physical and chemical factors (pH, temperature, Eh or the presence of vari-

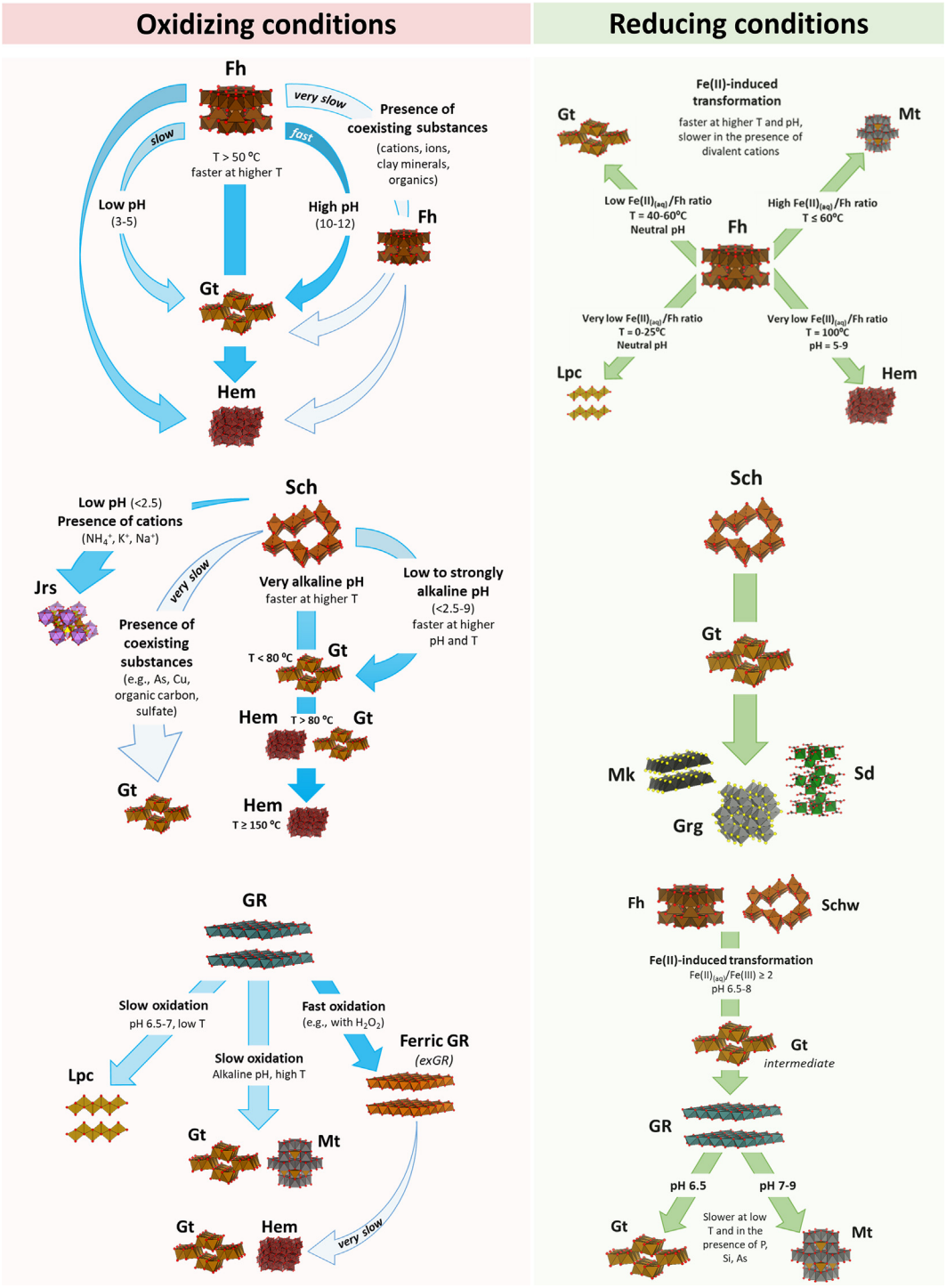

Fig. 6. (a) Documented pathways and mechanisms of Schw, Fh and GR transformation under oxidant and reducing conditions and the influence of physico-chemical conditions (e.g., pH, temperature, presence of ions and organics) on their transformation (see Section 1.3 for details). Note: Gt - goethite, Hem - hematite, Jrs - jarosite, Mk - mackinawite, Grg - greigite, Sd - siderite, Mt - magnetite, Lpc - lepidocrocite.

ous solutes like Si, Al, As, etc.), the synthesis procedure used and the allowed transformation time (Boland et al., 2014; Cornell et al., 1987; Das et al., 2011a; Hansel et al., 2005; Li et al., 2020; Liu et al., 2010, 2008; ThomasArrigo et al., 2019; Yee et al., 2006; Zhang et al., 2018a, 2018b, 2018c).

It is commonly accepted that under oxidizing conditions and in the presence of oxygen Fh transforms to goethite at acidic pH (3–5) and alkaline pH (10–12), and to hematite at near-neutral pH (7–8) at ambient temperature (Cudennec and Lecerf, 2006; Schwertmann et al., 2004, 1999; Schwertmann and Murad, 1983). At ambient temperatures, oxidazing conditions and circumneutral pH, Fh transformation can take months to years (Macera et al., 2020; Schwertmann and Murad, 1983). However, its transformation can be accelerated by increasing the pH and temperature in the absence of co-existing substances (Das et al., 2011a; Schwertmann et al., 2004; Schwertmann and Murad, 1983). At ambient temperature, Schwertmann and Murad (1983) observed that after 970 days the transformation of Fh was slow and 19% of

the initial Fh remained at pH $\leq$ 6 but less than 2% was found at pH $\geq$ 7. High temperatures increase the transformation rates, for example, at 92 °C Fh crystallization to hematite starts within 10 min (Johnston and Lewis, 1983). It was also observed that the increase of the temperature (50–100 °C) also favors Fh transformation to hematite irrespective of the pH (2–10) (Das et al., 2011a; Johnston and Lewis, 1983). This transformation has been suggested to occur via a two-stage crystallization process with goethite being intermediary, wherein both goethite and hematite were formed from Fh and with a transformation of goethite into hematite with the increase of the reaction time and temperature (Das et al., 2011a; Vu et al., 2008).

Fh transformation to lepidocrocite has been less studied (Liu et al., 2010), since lepidocrocite is assumed to be an oxidation product of Fe(II) (Cornell and Schwertmann, 2003). Some authors even suggested that lepidocrocite could never be formed from ferric species (Jolivet et al., 2006). Cornell et al. (1989a, 1989b) found that lepidocrocite could be a transformation product of Fh in the presence of L-cysteine. However, lepidocrocite was not detected in the presence of other organic ligands such as cysteamine or glutathione, etc. More recently, it has been found that under reducing and low oxygen concentrations and in the presence of trace of Fe (II) adsorbed on Fh it transforms rapidly not only into goethite and/or hematite but also magnetite and lepidocrocite (Boland et al., 2014; Hansel et al., 2005; Liu et al., 2010, 2007). The formation of lepidocrocite from Fh in the presence of Fe(II) is more favorable at low temperatures (0–25 °C), neutral pH (Liu et al., 2010, 2007), and in the presence of visible and solar irradiation (Shu et al., 2019). For the transformation from Fh to goethite, a moderate temperature (e.g. 40–60 °C) and a neutral pH value are the important factors, whereas the transformation to magnetite is favored by the presence of enough Fe(II) and temperatures of $\leq$ 60 °C, and the transformation of Fh to hematite could occur rapidly at pH 5–9 and $\sim$ 100 °C in the presence of trace Fe(II) (Liu et al., 2010). This aqueous Fe(II)-induced phase transformation could be an important driving force for Fh transformation in non-sulfidic anoxic soils, aquifers, and redox transition zones where the aqueous Fe(II), mainly generated by dissimilatory iron reduction, can be accumulated (Fei et al., 2018; Yee et al., 2006).

The presence of coexisting substances (e.g., ions, organic compounds, other minerals) also influences the transformation of Fh in natural environments (Cornell and Giovanoli, 1987; Cornell and Schneider, 1989; Cornell and Schwertmann, 1979; Das et al., 2011b; Gálvez et al., 1999; Li et al., 2020; Liu et al., 2016; Schwertmann et al., 2000; Vodyanitskii and Shoba, 2016; Yan et al., 2020; Zhang et al., 2018a, 2018b, 2018c). Although some coexisting substances (e.g., Fe^{2+}, cysteine) may accelerate the transformation of Fh by enhancing its dissolution–recrystallization process (Cornell and Schneider, 1989; Liu et al., 2016), inorganic cations, oxyanions, neutral small molecules, and natural polymers (generally adsorbed on the nanomineral surface) typically slow down its transformation by inhibiting the direct contact of the nanomineral surface with the solution and/or reducing its dissolution rate (Chen et al., 2015). As an example, divalent cations with higher binding abilities reduce the amount of bound-Fe(II) on Fh and inhibit its transformation rates (Chen et al., 2015; Cornell et al., 1987). Also, oxyanions such as arsenate, phosphate and silicate could be adsorbed onto Fh by inner-sphere complexes reducing its transformation rate by retarding Fh́s aggregation and dissolution (Cornell and Giovanoli, 1987; Das et al., 2011b; Gálvez et al., 1999). The presence of clay minerals favors the dispersion of Fh and the release of ions (e.g., Si and Al), decreasing its dissolution and reducing its transformation rates (Schwertmann et al., 2000). Therefore, in general, the presence of coexisting substances inhibits the direct contact and/or reduces the dissolution rate of Fh, decelerating its transformation rate (Cornell and Schwertmann, 2003).

1.3.2. Schwertmannite

The oxidative dissolution of sulfide minerals generates high concentrations of ferrous iron (readily transformed to ferric), sulfate and acidity. In these environments, the formation of Schw has been documented at pH values between 1.93 and 4.71 and sulfate concentrations between 7.4 and 97.34 mmol/L (Caraballo et al., 2013). Both biotic and abiotic oxidation of ferrous iron and direct ferric iron hydrolysis have been described (Asta et al., 2010a; Liao et al., 2009; Regenspurg et al., 2004). Schw is predicted to transform into more stable iron mineral phases such as goethite (α-FeOOH) (Acero et al., 2006; Bigham et al., 1996; Gagliano et al., 2004; Jönsson et al., 2005) or jarosite ($KFe_3(OH)_6(SO_4)_2$) (Acero et al., 2006; Kawano and Tomita, 2001) (Fig. 6). As it was mentioned for Fh, Schw transformation rate varies widely depending upon a range of physicochemical parameters (e.g., pH, temperature, ions and metals adsorbed onto the surface) as well as the activity of microorganisms (see, for example, the review of Paikaray (2020) and references therein). Specifically, under acid oxidizing conditions, its transformation proceeds over timescales of several months to years depending on the specific physicochemical conditions (Acero et al., 2006; Bigham et al., 1996; Jönsson et al., 2005, 2006; Kumpulainen et al., 2008; Regenspurg et al., 2004; Schwertmann and Carlson, 2005; Vithana et al., 2015) and goethite remains the most stable end-product (Bigham et al., 1996; Paikaray and Peiffer, 2012; Regenspurg et al., 2004). For example, Bigham et al. (1996) found that synthetic Schw completely transformed to goethite over 543 days; Acero et al. (2006), using natural Schw collected at a mine district in SW Spain, observed the formation of trace quantities of goethite as soon as after 105 days of aging Schw in its original solution. Further, Kumpulainen et al. (2008) reported that after one year of aging, only a synthetic Schw and one natural Schw had significantly transformed to goethite. Temperature and pH are key factors that control this transformation. Although Kumpulainen et al. (2008) described that the transformation rate becomes higher at low pH values, most of the studies have shown that the transformation rate increases with increasing pH and the concentration of $Fe(II)_{(aq)}$, and it is retarded at low temperatures (Burton et al., 2007, Jönsson et al., 2005; Knorr and Blodau, 2007; Schwertmann and Carlson, 2005). Schwertmann and Carlson (2005) reported that the transformation rate increased with increasing the pH from 4.0 to 7.2 and a complete Schw transformation to goethite in deionized water happened within 100 days. Regenspurg et al. (2004) observed significant, although incomplete, transformation of synthetic Schw over 362 days at pH 7. Jönsson et al. (2005) reported the conversion of Schw to goethite at pH 9 within 187 days while at pH 6 the conversion was still incomplete after 514 days. These authors also found that Schw did not transform for more than 5 years at a pH of 3 and a temperature of 4 °C. This temperature effect has been found more noticeable at highly alkaline conditions. For example, Davidson et al. (2008) found that goethite was formed in 200 min at 60 °C and in 30 min when the temperature was increased to 80 °C at pH 13.2. These authors also reported the formation of goethite as the only crystallization product at temperatures $\leq$ 80 °C, while at temperatures greater than 80 °C goethite and hematite formed almost simultaneously, and at temperatures $\geq$ 150 °C goethite was transformed to hematite.

Schw transformation rate and the end-product formed are also affected by the solution composition. The presence of some cations that are part of jarosite crystal structure (e.g., K^+, NH_4^+, or Na^+) promotes Schw transformation to this mineral at solution pH values lower than 2.5 (Acero et al., 2006; Kumpulainen et al., 2008). However, in the absence of these cations and at solution pH values close

to 3.5, goethite forms instead (Schroth and Parnell, 2005). Furthermore, the solution composition can also remarkably enhance Schw stability due to the sorption of dissolved species like arsenic, chromate, phosphate, copper or dissolved organic carbon (Antelo et al., 2013; Asta et al., 2010b; Cruz-Hernández et al., 2017; Fukushi et al., 2003; Khamphila et al., 2017; Knorr and Blodau, 2007; Paikaray and Peiffer, 2012).

On the other hand, Schw transformation under reducing conditions has received less attention (Blodau, 2006). Under such conditions, microbial iron reducers and sulfate reducers could use Schw-derived Fe(III) and sulfate as electron acceptors during the degradation of the organic matter (Blodau and Gatzek, 2006) triggering the reductive dissolution of Schw. This process raises the pH, favoring Schw transformation into more stable goethite, and releasing sulfate which can be subjected to dissimilatory sulfate reduction. Natural profiles of acidic sediments and wetlands and laboratory studies have shown that over time Schw tends to be replaced by goethite and eventually by reduced Fe and S phases formed by sulfate reduction coupled to the reductive dissolution of goethite by H_2S at depth (Burton et al., 2007, 2006; Gagliano et al., 2004; Peine et al., 2000; Schoepfer et al., 2019).

1.3.3. Green rust

In the case of GR phases, they commonly form in anoxic and non-sulfidic environments via the Fe^{2+}-catalyzed transformation of metastable Fe(III)-bearing minerals such as Fh and Schw between pH 7 to 8.5 (Ahmed et al., 2010; Usman et al., 2012; Perez et al., 2021b). In those settings, GR phases often subsequently transform to magnetite via dissolution-precipitation pathway (Sumoondur et al., 2008; Perez et al., 2021a; Perez et al., 2021b; Yutaka et al., 1984). Sumundoor et al. (2008) studied magnetite formation via a GR intermediate using in situ synchrotron-based X-ray scattering. Their results showed that the Fe(II)/Fe(III) ratio and pH controlled the rate of GR transformation to magnetite. Complete conversion to magnetite (see Fig. 6) was only observed at slightly alkaline conditions (pH 9), and higher Fe(II)/Fe(III) ratios resulted in fast transformation rates (greater than 99% conversion within 2 h at Fe(II)/Fe(III) = 2). It must be noted that this study was performed using ultrapure water, and water chemistry can influence the GR transformation. In a recent study by Perez et al. (2021a), synthetic GR sulfate (GR_{SO4}) was aged anoxically in a natural groundwater ($[HCO_3^-]$ = 4.5 mM, [Si] = 0.6 mM] at ~ 25 and 4 ℃. Aging synthetic GR_{SO4} at 25 ℃ led to its partial conversion to GR carbonate (GR_{CO3}) via ion exchange, followed by gradual transformation to magnetite after 15 days until its completion after 120 days. Lower aging temperature (i.e., 4 ℃), however, slowed down these transformation rates, with GR_{CO3} only appearing after 60 days and only trace amounts of magnetite even after one year.

Meanwhile, controlled air oxidation of GR phases in aqueous media (see Fig. 6) results in the formation of secondary Fe (oxyhydr)oxides such as lepidocrocite, goethite and/or magnetite, which is heavily influenced by pH, temperature and rate of oxidation. Lepidocrocite is a common GR oxidation product under circum-neutral pH (6.5–7) and low temperature (Schwertmann and Fechter, 1994; Nagata et al., 2009; Wang et al., 2013), while alkaline pH and high temperature usually results in the formation of magnetite and/or goethite (Feng et al., 2015; Wang et al., 2013). It is noteworthy that these transformation reactions all proceed via dissolution-oxidation-precipitation mechanism. However, if oxidized very quickly (e.g., chemical oxidation using H_2O_2), it is possible to fully oxidize all the structural Fe(II) sites in GR while retaining original morphology and crystal structure (i.e., solid-state oxidative transformation, Fig. 6; Génin et al., 2005; Refait et al., 2003). These ferric GR phases (sometimes called exGRs) are still made up of pure Fe(III) hydroxides sheets with intercalated anions and water molecules with same stacking arrangements (Génin et al., 2006). However, the crystal lattice is contracted with ~ 5% decrease in *a* and ~ 3% decrease in *c* (Abdelmoula et al., 1996; Génin et al., 2006) due to the smaller ionic radii of $Fe(III)_{oct}$ (0.645 Å) compared to $Fe(II)_{oct}$ (0.78 Å) (Shannon, 1976), and the $Fe(III)_{oct}$ is deprotonated to compensate for electrical neutrality in the crystal structure (Mullet et al., 2008). Upon prolonged aging, however, exGRs eventually transform to goethite and/or hematite (Legrand et al., 2004; Antony et al., 2008).

Similar to other Fe (oxhydr)oxides, the presence of oxyanions can slow down or even inhibit the rate of GR transformation. Dissolved phosphate (Benali et al., 2001; Bocher et al., 2004; Hansen and Poulsen, 1999), silica (Kwon et al., 2007; Sahoo et al., 2011) and arsenate (Perez et al., 2020; Wang et al., 2014; van Genuchten et al., 2019) sorbed onto GR particle edges have all been shown to increase solid phase stability by preventing crystal dissolution. Metal substitution in the Fe hydroxide sheets of GR can also alter the resulting oxidation end-products. Wang et al. (2019) showed that the oxidative transformation of metal substituted GR to goethite via lepidocrocite depends on the complexation constants of the divalent cations (Cu^{2+} > Ni^{2+} > Mn^{2+}), wherein larger complexation constants led to faster goethite transformation.

These three metastable iron-bearing nanominerals shows some common behavior regarding their transformation to more stable iron minerals. Generally speaking, if the metastable nanominerals are maintained within their predominance fields (Fig. 1b, 1c) by keeping their original hydrochemical forming environment (i.e., pH, pe, dissolved elements variety and concentration, P and T), their transformation to other stable mineral phases is highly slowed (taking from years to decades). However, any perturbation of one or more of these original forming conditions automatically favors a fast transformation of these metastable nanominerals to more stable iron minerals phases (taking just from days to months).

As previously shown, GR is typically formed under reducing or slightly oxidizing environments (Fig. 1b) whereas the most common final stable iron minerals (i.e., hematite, magnetite, goethite and lepidocrocite) are formed at oxidizing environments. Therefore, the transformation of GR to more stable iron minerals is highly enhanced by a change in the redox potential of the solution (i.e., towards a more oxidizing environment), whereas the transformation rate of Fh and Schw, which are formed at oxidizing environments, is not much affected by a change in that parameter (i.e., towards a more reducing environment). On the other hand, Fh and Schw transformation rates seem to be highly affected by the changes of the solution pH (Fig. 6) whereas this parameter does not affect as much the transformation rate of GR (partially due to its narrow pH stability range).

Another common behavior for these metastable iron-bearing nanominerals is that the presence of sorbed oxyanions (e.g., silicate, phosphate, arsenate, chromate or organic molecules) can slow down or even inhibit their transformation rates (Fig. 6). Similarly, the presence of certain amounts of cations, like Si^{4+}, Al^{3+}, Cu^{2+}, Ni^{2+}, Mn^{2+}, K^+, NH_4^+, or Na^+ in their crystal structure or in the solution in contact with the nanomineral, may have an impact in the specific stable iron-bearing mineral resulting from the transformation.

2. Presence and relevance of Fe nanominerals in past and present earth environments

Of the almost 10,000 publications covering one or more of these three iron-bearing metastable nanominerals, a high percentage (probably a few thousands) of these mentions or discusses their presence and role in natural environments. As a result, the following section is not intended to be a comprehensive presentation of

all these publications, but rather a schematic summary of the most relevant natural environments where one or more of these nanominerals have been reported as major players in the iron biogeochemical cycle. Also, the reader is referred to some of the many outstanding works presenting the fundamentals of the iron biogeochemical cycle (e.g., Raiswell and Canfield, 2012; Hamilton et al., 2020, and references therein) to get a broader understanding (not so focused on iron-bearing nanominerals) of this topic. As a general statement: one or more of the three metastable iron-bearing nanominerals is most probably the predominant neoformed mineral phase in natural or anthropogenic waters, close to environmental conditions (25 °C and 1 atm) and at oxidizing or slightly reducing conditions, which hydrogeochemistry is controlled by the iron biogeochemical cycle. As a result, these nanominerals are ubiquitous on Earth's surface (as it will be shown) and their limited recognition is mainly due to their poor crystallinity, metastability and nanosize, and the inherent difficulties to properly sample and unambiguously identify them using the current most available analytical techniques (see Fig. 7).

2.1. Present earth

2.1.1. AMD and ARD environments

Acid mine drainage (AMD) and acid rock drainage (ARD) systems are without any doubt the "kingdom" of the iron metastable nanominerals, because these anthropogenic and natural environments have the perfect hydrogeochemical conditions for the neoformation and preservation of these nanominerals. Consequently, the numerous complex mechanisms and hydrogeochemical process, by which these iron metastable nanominerals control the hydrogeochemistry of these waters, have been addressed by an abundant record of publications over the last four decades (Bigham and Nordstrom, 2000; Blowes et al., 2003 and references therein). The neoformation of Fh, Schw, or GR are primarily controlled by the water pH and pe (Fig. 1) and by the specific chemical composition (e.g., the presence of sulfate or carbonate will control the type of GR). Generally speaking, acidic (pH 2 to 4.5), oxidizing (pe 6 to 18) sulfate and Fe-rich waters (by far the most common conditions in AMD/ARD affected sites) is the realm of Schw (Fig. 1c); slightly acid to basic (pH 4.5 to 10), oxidizing to slightly reducing (Eh 1 to 0.2 V) iron rich waters is the domain of Fh; and almost neutral to basic (pH 6.5 to 10), slightly oxidizing to reducing (Eh 0.1 to −0.6 V) iron rich waters is the field of GR (Fig. 1b). The most common generic settings will be highlighted among the thousands of specific locations where iron metastable nanominerals have been reported. The three nanominerals have also been reported in AMD/ARD affected rivers (Asta et al., 2010a, 2010b; Dekov et al., 2014; Johnson, et al., 2014) and lakes (Sánchez-España et al., 2011; Vuillemin et al., 2019, Castendyk and Webster-Brown, 2007). In addition, these nanominerals has been

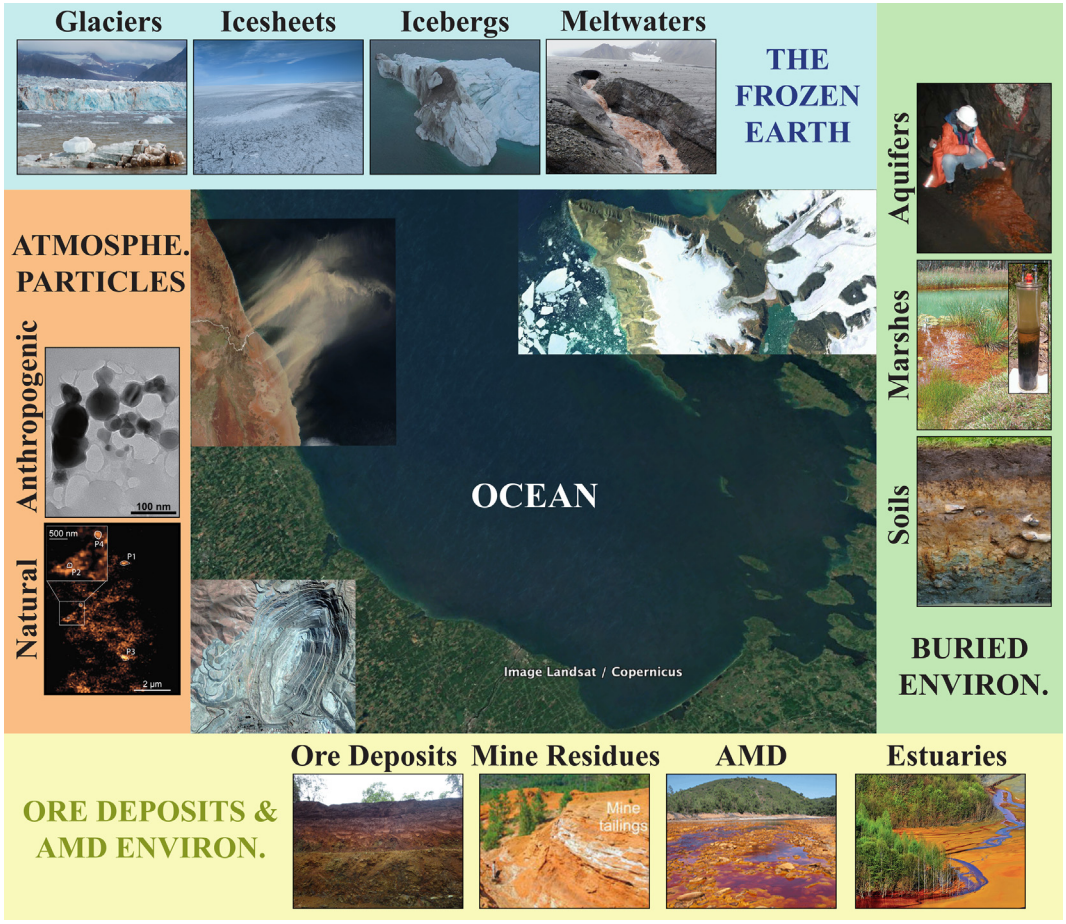

Fig. 7. Schematic representation of the multiple surface Earth environments where Fh, Schw and GR have been reported to play an important role in the iron biogeochemical cycle. Photo credits from top-left, clockwise: (i) Adapted from Jørgensen et al. (2021) and reproduced with permission from John Wiley & Sons.; (ii) Photo courtesy of C. Trivedi; (iii) Adapted from Carlson et al. (2019); (iv) Raiswell and Canfield (2012); (v) Christiansen, 2008; (vi) Adapted from Schoepfer and Burton (2021) and reproduced with permission from Elsevier; (vii) Photo courtesy of S. Polte, Boden des Jahres 2016 (Deutsche Bodenkundliche Gesellschaft); Adapted from Vaziri Hassas et al. (2020) and reproduced with permission from Elsevier; (viii) Adapted from Sanz et al. (2011) and reproduced with permission from John Wiley & Sons; (ix) Modified from Martín-Crespo et al. (2020); (x) Adapted from Delina et al. (2020) and reproduced with permission from Elsevier; (xi) Adapted from Hawkings et al. (2018); (xii) Adapted from Adachi et al. (2021).

reported as alteration product of multiple types of sulfide bearing residues like tailings (Kawamoto et al., 2021; Dold and Fontboté, 2002, Dore et al., 2020) and waste rock dumps and spoil heaps (Koski et al., 2008; Smuda et al., 2007), as well as AMD affecting both natural groundwater (Johnson et al., 2014) and treatment plants (Filip et al., 2007; Caraballo et al., 2009, Bearcock et al., 2011).

2.1.2. The frozen Earth

Fh has been extensively reported as an authigenic mineral in icebergs and glaciers at Arctic and Antarctic locations in subglacial sediments (Raiswell et al. 2016 and references therein). It has also been proposed as the predominant component of the particulate bioavailable iron pool in Greenland meltwaters and ice sheets (Bhatia et al., 2013, Hawkings et al., 2014). Bhatia et al. (2013) estimated that bioavailable iron from glacial runoff in Greenland is about 0.3 Tg/year, whereas Hawkings et al. (2014) estimations are in the range of 0.4 to 2.54 Tg/year. In both cases this is comparable to dust-derived soluble iron inputs to the North Atlantic. Fh have also been reported as playing an essential role controlling the natural remediation and the transport of metallic contaminants in boreal streams with high organic matter content (Köhler et al., 2014). Schw has been reported as a result of ARD generation in regions with abundant snow and/or ice in the Antarctica (Dold et al., 2013), or in wet, acid, and oxic microenvironments beneath polar and polythermal glaciers (Raiswell et al., 2009) in the Antarctica and the Svalbard islands (Norway). Recently, Hawkings et al. (2018) documented the widespread occurrence of amorphous and Fe(II)-bearing nanoparticles in Arctic glacial meltwaters and iceberg debris. Although they were not able to assign a specific iron-bearing nanomineral to their discovery, their findings suggest that GR phases may have an important role in those environments that will most probably be confirmed by new studies in the near future.

2.1.3. Buried environments

Buried environments like soils, groundwaters and wetlands are transitional environments that typically show redox potential grading moving from oxidizing to reducing environments. In addition, they most commonly exhibit significant contents of organic matter. Fh is typically the most frequent metastable iron-bearing nanomineral in those environments, followed by GR and Schw.

Fh is one of the most common Fe mineral phases controlling the iron biogeochemical cycle in many different types of soils (e.g., podzolic-, arable-, gleyic-, sandy- or acidic-soils, Vodyanitskii and Shoba, 2016 and references therein); whereas Schw is more predominant in acid sulfate soils (Burton et al., 2007; Collins et al., 2010). On the other hand, GR is most frequent in poorly drained soils (e.g., gleysols and reductisols; Trolard et al., 1997), where the precipitation of this nanomineral is intimately related to the activity of iron reducing bacteria (Berthelin et al., 2006). The three metastable iron-bearing nanominerals are frequently found in wetlands where the whole cycle of neoformation and transformation between them along the depth redox profile can be observed (Karimian et al., 2018). These nanominerals play an essential role in contaminant immobilization, like As and Se, in wetlands and soils (Karimian et al., 2018). The presence of Fh and other iron minerals (like goethite) in aquifers is very common and it has been directly related to the sorption/desorption of pollutants like As (Polizzotto et al., 2006). GR identification in groundwaters is quite challenging due to its rapid oxidation and transformation within a few minutes after sampling. Because of that, the number of studies reporting GR in groundwaters are limited but they are growing after the publications of sampling and preservation methods like the ones proposed by Christiansen et al. (2009a) and Johnson et al. (2014). The former was able to identify GR in samples taken below the water table from a fractured granite, and the latter from groundwater flowing to the surface around a former uranium mine. On the other hand, the presence of Schw in groundwaters is limited (Blodau, 2004) because these waters easily transition to more reducing conditions where Schw becomes unstable compared with other iron-bearing nanominerals like Fh or GR.

2.1.4. Atmospheric particles

Mineral dust from desert regions are typically composed of several Fe-bearing minerals including Fh and other poorly crystalline Fe phases, hematite, goethite, magnetite and Fe-bearing clay minerals (Shi et al., 2012), but excluding Schw or GR. Shi et al. (2011) reported that, among all those iron-bearing mineral phases, Fh is probably one of the most important ones forming the highly reactive Fe pool in the Saharan dust samples. In regions where volcanoes can be an important source of mineral dust, that group of Fe-bearing minerals are absent from freshly-erupted ash (Ayris et al. 2012). However, these phases may form thanks to different processes, like the generation of Fh due to the atmospheric near-neutral pH values achieved at the surface of the ash during cloud forming processes (Shi et al., 2011). Similarly, Takahashi et al. (2013) showed that the main Fe phases in aerosols in the Northwest Pacific region (i.e., Tsukuba, Japan) correspond to illite, hornblende, Fe(III) sulfate and Fh. They proposed that the source of Fh is most probably the soil around the sampling site, although it could also be formed by acid processing in the atmosphere. Regarding anthropogenic dust, magnetite has been reported as the most ubiquitous iron mineral phase in pyrogenic aerosols whereas Fh, Schw or GR has not been detected (Ito et al., 2021). However, the presence of these iron-bearing nanominerals, especially Schw, at local or regional scales could be expected (and should be further studied) at big mining districts (Sanchez de la Campa 2020).

2.1.5. Ocean

AMD or ARD waters are often subjected to abrupt hydrochemical changes in estuaries due to their mixture with high salinity and neutral pH sea waters. As a result, immediate removal of iron (and other metals) through intense precipitation of Schw and Fh has been proposed (Asta et al., 2015), and the presence of these nanominerals in the estuary sediment has been reported (Abramov et al., 2020). Regarding GR in estuaries, one of the very few studies (Jorand et al., 2011) suggested the biomineralization of this nanomineral in the ferruginous biofilms at the Sinnamary Estuary (French Guiana). The presence of Fh in North Sea sediments was proposed almost 3 decades ago by Slomp et al. (1996) and since then it has been reported in many other sea sediments around the world, like the study of Lenstra et al., (2019, and references therein) presenting a new model for the shelf-to-basin iron shuttle in the Black Sea. These authors also demonstrated the presence of Fh in the water suspended particles reaching the Black Sea. To the best of our knowledge, the presence of Schw or GR has not been reported yet in sea sediments or in suspended particles in sea water (apart from their presence at estuarine environments). However, because of the growing recognition of other nanominerals (Silva et al., 2021a,b; Oliveira et al., 2021b) and these specific iron-bearing nanominerals in oceanic input sources like atmospheric dust, glacier, ice sheet and iceberg sediments and rivers, the emergence of many new studies covering this gap is foreseen.

It is important to emphasize that despite the abundance of studies identifying Fh, Schw, or GR in multiple Earth natural and anthropogenic environments, an even higher number of studies highlight the importance of "*unidentified*" iron-bearing nanoparticles or nanominerals as bioavailable sources of iron in seawaters (von der Heyden et al., 2012), meltwaters (Bhatia et al., 2013) and glacial sediments (Hawkings et al., 2018); metal pollutant nanovectors in soil-river systems (Hassellöv and von der

Kammer, 2008) or iron-rich sediments in water reservoirs (Root et al., 2007), among many others. Hence, it is reasonable to assume that the number of studies reporting the presence of these iron metastable nanominerals on Earth will keep increasing. This is all thanks to an increase in the access to current sophisticated characterization equipment (e.g., HRTEM or Synchrotron based spectroscopies) and to the reassessment of old data based on new knowledge.

2.2. Earth in the past

Iron metastable nanominerals can be considered short-lived minerals (on a geological time scale). They can only be found in geologically young strata (less than 10,000 years old) if their mineral transformation to more crystalline iron mineral phases has been inhibited or significantly retarded (Cornell and Schwertmann, 2003 and references therein). Banded iron formations (BIFs) are distinctive rock formations consisting of alternating layers of Fe-rich and Si-rich bands that have been deposited in the early Earth's oceans about 3.8 to 0.6 billion years ago (Bekker et al., 2010; Poulton and Canfield, 2011). Due to their chemical and mineralogical alterations resulting from deposition and diagenesis (Bekker et al., 2014; Klein, 2005), the pathways leading to their formation are still poorly understood, and their early Fe mineral precursors are still debated (Rasmussen et al., 2014). Earlier studies (e.g., Bjerrum and Canfield, 2002; Posth et al., 2013) have suggested poorly ordered phases such as ferrihydrite, hydrous ferric oxide (HFO), or an Fe(III)-Si gel, formed by the (abiotic or biotic) oxidation of dissolved Fe^{2+} in the redoxcline. However, more recent studies have indicated that mixed-valence Fe phases such as GR and greenalite may have played an important role in the genesis of BIFs (Johnson et al., 2018). In particular, GR phases have been proposed to have contributed to Fe cycling in our ancient oceans (Halevy et al., 2017; Russell, 2018), a process that was compared to their existence in modern non-sulfidogenic ferruginous lakes (e.g., Koeksoy et al., 2019; Vuillemin et al., 2019; Zegeye et al., 2012). The formation of Fh and GR in these ancient oceans would have dramatically impacted the cycling of nutrients (e.g., P, Ni; Jones et al., 2015; Eickhoff et al., 2014) and toxins (e.g., As; Chi Fru et al., 2016), resulting in the chemistry and associated microbial life signals preserved in BIFs today (Kappler et al., 2005; Konhauser et al., 2002; Posth et al., 2013). A recent study (Barge et al., 2019) has also suggested that, along with redox and pH gradients, GR phases could have contributed to the synthesis of prebiotic organic molecules (e.g., amino acids) necessary for the emergence of early ancient life (Duval et al., 2019; Russell, 2018). Schw and Fh have also been proposed to be mineral precursors of other more stable phases like goethite in Gossan type deposits in arctic environments (West et al., 2009).

2.3. Extraterrestrial

Extraterrestrial occurrence of Fh has been reported or suggested in meteorites (Beck et al., 2015; Brearley, 1997, 1989; Greshake, 1997; Keller and Buseck, 1990; Muttik et al., 2014; Tomeoka and Buseck, 1988; Treiman et al., 2014) and in interplanetary dust particles (Matrajt et al., 2002; Nakamura et al., 2004). Two-line Fh was found for the first time as a major constituent of the matrix of a chondrite (Orgueil meteorite) by Tomeoka and Buseck (1988). They suggested a preterrestrial ferrihydrite origin rather than a terrestrial weathering product in this meteorite, although in other carbonaceous chondrites terrestrial weathering might also have occurred after the meteorite fell to Earth (Brearley, 1997; Greshake, 1997). Fh also occurs in Martian meteorites (Lafayette, "Black Beauty") (Beck et al., 2015; Muttik et al., 2014), and has long been suspected to be present on the surface of Mars based on spectroscopic comparisons (e.g., Bishop et al. (1993), Morris et al. (1993)). Recently, geochemical and mineralogical data collected by in situ missions have brought new evidence of the presence of nanocrystalline iron-rich phases in Martian soils and sedimentary rocks and suggest the widespread presence of ferrihydrite on Mars (Dehouck et al., 2017). The presence of Schw was suggested as a component in Meridiani outcrop materials (Farrand et al., 2009) and the Meridiani Planum region (Bibring et al., 2007). After that, it has become a keystone mineral phase in several studies that model the current mineral composition of the Martian surface. These models incorporate schwertmannite as a metastable precursor to other mineral phases like jarosite or goethite (Tosca et al., 2008; Hurowitz et al., 2010). Liu et al. (2018), in their spectral and stratigraphic mapping of hydrated minerals associated with interior layered deposits near the southern wall of Melas Chasma, Mars, also proposed that the major end-members that are mixed with jarosite in their study area may be Fh (with an abundance of ~30% for unit 1) and Schw (with an abundance of ~35% for unit 2).

3. Fe-bearing nanominerals present and future technological applications

3.1. Emerging contaminant treatment by Fenton reactions

Emerging contaminants (EC) can be understood as any previously unknown contaminant (or any chemical compound not yet recognized as a contaminant), whose presence in the environment does not have to be new but the concern about its possible toxic consequences does. ECs originate from anthropogenic and natural compounds, including personal and industrial care products, pharmaceuticals, pesticides, hormones, plastic products, among others (Gavrilescu et al., 2015). These compounds are very dangerous, mainly because they can accumulate in the human body and they are endocrine disrupting chemicals (EDCs) (Yousefi et al., 2019). Advanced oxidation processes such as photochemical oxidation, wet catalytic oxidation, sonochemical oxidation, ozone oxidation, electrochemical oxidation and Fenton oxidation have been widely used in recent decades for the degradation and/or complete mineralization of various types of organic pollutants. Among all of them, homogeneous Fenton-type processes have gained great popularity mainly due to the fact that they are simple to operate, generate rapid degradation and have a wide application range (Bokare and Choi, 2014; Sharma et al., 2018; Zhang et al., 2019). As shown in the Fenton reaction (Eq. (1)), ferrous iron is oxidized, in the presence of hydrogen peroxide, with ferric iron and hydroxyl radical (•OH) produced.

$$Fe^{2+} + H_2O_2 + H^+ \rightarrow Fe^{3+} + H_2O + \bullet OH \quad (1)$$

This free radical has a great oxidative capacity, inducing a fast degradation of most organic pollutants to CO_2 and H_2O (Santos et al., 2011). In addition, the last decade has seen a significant increase in the number of scientific studies applying heterogeneous Fenton process to degrade very different pollutants (Kantar et al., 2019; Liu et al., 2017; Meng et al., 2020; Yang, 2019; Zhang et al., 2018a, 2018b, 2018c). In this new approach, the dissolved Fe^{2+} catalyst used in the homogeneous Fenton system is replaced by a solid catalyst that contains active catalytic compound able to generate hydroxyl radicals in a Fenton-like reaction (i.e., Fe^{2+}, Fe^{3+} or some other metals). The big difference is that the catalytic reactions occur at the active sites on the surface of the solid catalyst, avoiding the leaching of iron ions with the concomitant reduction of iron sludge and the extension of the working pH range (Liu et al., 2017).

Among the multiple chemical reagents used in pure heterogeneous Fenton-type strategies or hybrid homogeneous/heterogeneous strategies, it is noticeable to see the recent boom in the use of minerals (as solid catalysts) for the sake of a more sustainable approach to this problem. Most studies use sulfides, mainly pyrite (Meng et al., 2020; Yang, 2019), and GR (Kone et al., 2009; Hanna et al., 2010) as a source of Fe^{2+}, or sulfates and oxides (mainly schwertmannite, $Fe_8O_8(OH)_8(SO_4)\cdot nH_2O$); and goethite, FeOOH) as a source of Fe^{3+} (Kantar et al., 2019; Zhang et al., 2018a, 2018b, 2018c). However, the vast majority of studies to date are based on synthetic (non-natural) mineral samples that have been used to study the degradation of a single EC under very limited operational conditions and on a laboratory scale.

On the other hand, it has to be considered that the mining industry processes (globally) millions of tons of ore daily, generating a large amount of primary wastes. More than 95% of these are deposited as dumps or tailings (Falagán et al., 2017), generating between 5 and 7 billion tons of mine tailings annually worldwide (Edraki et al., 2014). Tailings and mining dumps usually contain potentially toxic metals and metalloids such as As, Cd, Cu, Fe, Ni, Pb, Sb and Zn (Anawar 2015), which can occur in high concentrations, reaching in some cases values between 0.3 and 5 wt% (Falagán et al. 2017). In addition, oxidation of iron sulfides (typical mineral phases contained in these mine residues) generates AMDs that are waters with low pH and high metal and sulfate contents (Younger et al., 2002). These AMD waters typically generate metastable iron-bearing nanominerals (i.e., Fh, Schw, GR) that will eventually transform to jarosite and goethite under surficial environmental conditions (Bigham and Nordstrom, 2000). These secondary mine residues can be categorized as natural, like the sediments in rivers and lakes contaminated by AMD, or anthropogenic, like the precipitates formed after the active (Younger et al., 2002) or passive (Ayora et al., 2013) treatment of these polluted waters. As a result, metallic mining districts are characterized worldwide by the presence of gigantic stacks of primary and secondary mine residues that typically generate important environmental and health problems.

Taking into account these two realities (i.e., the significant state of progress shown by the treatment of EC using synthetic iron-bearing nanominerals, and the vast amount of natural and anthropogenic iron-bearing nanominerals), it is reasonable to expect that many new research projects linking the two of them will appear in the near future.

3.2. Applications based on high sorption capacities of Fe-bearing nanominerals

Sorption capacities of metastable Fe phases have been extensively studied during the last decades, and many sorption isotherms have been published (Bigham and Nordstrom, 2000; Cornell and Schwertmann, 2003, among many other studies). However, most of these studies have focused on the sorption of heavy metals and metalloids cations and anions typically present in AMD like arsenic, chromium, antimony or fluoride, among others (Zhang et al., 2018a, 2018b, 2018c; Shi et al., 2021 and references therein). As a result, whereas the geochemical and mineralogical mechanisms controlling metals and metalloids sorption onto the metastable iron-bearing nanominerals (as well as onto other iron minerals) comprising AMD precipitates is well understood, those mechanisms are still poorly known for most organic pollutants as well as for other relevant inorganic pollutants like NO_3^- and PO_4^{2-}. The topic of organic pollutants sorption capacities has been systematically overshadowed by the search of efficient heterogeneous Fenton-like reactions to mineralize the organic pollutants (Section 3.2.1), because as soon as the pollutants reach the iron-bearing nanomineral surface, the degradation reaction takes place. Regarding NO_3^- and PO_4^{2-}, best management practices (BMPs) have been widely implemented to treat stormwater runoff and agricultural discharges (Urbonas and Stahre, 1993). Some BMPs involve employing green sorption media (GSM) to help remove nutrients in stormwater runoff and agricultural discharge in any landscape (Wen et al., 2020). The materials used for the development of green sorption media mixes are intended to be cost-effective and sustainable due to their use via recyclable materials, and renewable due to possible nutrient recovery (Ordonez et al., 2020). Among the various type of water filtration materials (e.g., coconut coir, expanded clay, tire crumb, activated carbon, bark, corn stover and biomass bottom ash, among others), synthetic iron filings (Wei et al., 2008) and Fe-rich sludge from AMD treatment facilities (Wen et al., 2020; Sibrell et al., 2009) are being used. However, most sorption treatments using Fe-rich sludge are focused just in PO_4^{2-} but none of them study NO_3^- sorption. In addition, the specific mineralogical composition of the Fe-rich sludge used to treat PO_4^{2-} is continuously neglected and only the bulk chemistry of the residue is considered (Sibrell et al., 2009; Wei et al., 2008; Wen et al., 2020). As a result, the sorption capacity of the bulk material is characterized, but the real sorption capacities of the different mineralogical phases comprising the sludge is ignored. It also has to be considered that nitrate and/or phosphate pollution of surficial waters and groundwaters typically induce an uncontrolled bloom of algae and microalgae. When these dense algal blooms eventually die, microbial decomposition severely depletes dissolved oxygen, creating a hypoxic or anoxic 'dead zone' lacking sufficient oxygen to support most organisms (Chislock et al., 2013). Eutrophication is frequently related to excessive or inefficient fertilization of agricultural fields (Andujar et al., 2006; Paredes et al., 2020). However, there are some other sources like untreated wastewater discharges (Paredes et al., 2020), uncontrolled leachates from phosphogypsum stacks (Barba-Brioso et al., 2010; Pérez-López et al., 2016) and aquaculture effluents from fishery (Sibrell and Kehler, 2016) that must not be ignored. According to Dodds et al. (2009), the economic cost of water eutrophication in the United States is approximately $2.2 billion per year.

Taking into account the significant sorption capacity exhibited by metastable iron-bearing nanominerals, the vast amount of natural and anthropogenic iron-bearing nanominerals and the frequent eutrophication problems (induced by anthropogenic uncontrolled emission of NO_3^- and PO_4^{2-}) suffered worldwide, a broader reuse of these mine residues, under a circular and green based economy, is foreseen.

3.3. Other uses and applications:

Based on the results offered by some recent exploratory studies (Lozano et al., 2020), Schw and Fh could potentially be a source of some critical raw elements. They could be enriched in rare earth elements (REEs), depending on the elemental composition and the physicochemical parameters of the waters where they were formed, by using them as sorbet phases to trap valuable elements from AMD and/or ARD. However, the same authors also proposed hydrobasaluminite (an aluminum hydroxysulfates nanomineral) as the main mineral actually involved in REE trapping through mineral precipitations at AMD natural and engineered settings (Ayora et al., 2016; Lozano et al., 2020).

Many studies have shown during the last decades that iron, an essential micronutrient, can inhibit or boost microalgae growth (Smetacek et al., 2012). It is common knowledge that microalgal photosynthesis uses $CO_{2(g)}$ to produce $O_{2(g)}$ and the organic molecules comprising their organism, resulting in a net $CO_{2(g)}$ removal from the atmosphere when the microalgae die and are transported and stored in the deep sea. As a result, the idea of fertilizing the oceans using different sources of iron as a geoengineer strategy

to remove atmospheric $CO_{2(g)}$ arose some decades ago and it has been tested in situ (Boyd and Ellwood, 2010) or modeled (Aumont and Bopp, 2006). Given the high abundance, worldwide distribution and high solubility at alkaline conditions of metastable iron-bearing nanominerals (especially for Schw), their use as nutrient seeds to foster algae growth in geoengineering strategies could become a future application of these nanominerals.

4. Conclusions and perspectives

As it has been shown throughout this review, the three metastable Fe-bearing nanominerals presented (i.e., Fh, Schw and GR) are both intimately related themselves and as precursors of other more crystalline and stable Fe-bearing minerals like goethite, lepidocrocite, hematite or magnetite. The combined study of these three nanominerals clearly exemplifies how the disorder of a metastable nanomineral crystal structure increases as its crystallinity decreases, resulting in bulk chemistries and solubility products spanning unusually broad ranges. This observation has deep implications in the hydrochemical modelling of water environments controlled by the precipitation/dissolution of these nanominerals, because the equations used in these models typically require the use of a single representative solubility product for a specific chemical reaction including a single bulk chemistry of the nanomineral. In the same line of reasoning, the generation of theoretical values (using the nanomineral modeled crystal structure) of their physicochemical properties (e.g., sorption capacity, density, etc.) also becomes virtually impossible, resulting in the need to rely on the heterogeneous (and frequently discrepant) experimental measurements of these parameters.

These three metastable iron-bearing nanominerals show some common behaviors regarding their transformation to more stable iron minerals. Generally speaking, if their original hydrochemical forming environment (i.e., pH, pe, dissolved elements variety and concentration, P and T) is maintained, their transformation to other stable mineral phases is greatly retarded (taking from years to decades). However, any perturbation of one or more of these original forming conditions automatically favors a more rapid transformation to more stable iron minerals phases (taking just days to months). Another common behavior is that the presence of sorbed oxyanions (e.g., silicate, phosphate, arsenate, chromate or organic molecules) can slow down or even inhibit their transformation rates. In contrast, the presence of cations (e.g., Si^{4+}, Al^{3+}, Cu^{2+}, Ni^{2+}, Mn^{2+}, K^{+}, NH_4^{+}, or Na^{+}) in their crystal structure or in solution may have an impact on the specific stable iron-bearing mineral resulting from the transformation.

As has been shown, this group of iron-bearing metastable nanominerals are widely present on currently existing Earth (and Mars) surface environments as well as on similar past environments where the iron cycle is or was a predominant geochemical cycle. Also, it is envisioned that the number of studies reporting the presence of these iron metastable nanominerals will keep increasing as many of the reported (and future) "*unidentified*" iron-bearing nanoparticles or nanominerals are finally classified as Fh, Schw or GR. By the same token, the multiple technological- and environmental-related applications currently under development are expected to grow and to diversify as the scientific understanding of these metastable iron-bearing nanominerals increase, and as more and more geochemical/mineralogical processes are observed in nature and properly described and understood.

CRediT authorship contribution statement

Manuel A. Caraballo: Conceptualization, Visualization, Writing – original draft, Writing – review & editing. **Maria P. Asta:** Visualization, Writing – original draft, Writing – review & editing. **Jeffrey Paulo H. Perez:** Visualization, Writing – original draft, Writing – review & editing. **Michael F. Hochella:** Writing – original draft, Writing – review & editing.

Declaration of Competing Interest

The authors declare that they have no known competing financial interests or personal relationships that could have appeared to influence the work reported in this paper.

Acknowledgments

This research was partially supported by Advanced Mining Technology Center (AMTC) from Universidad de Chile; National Agency for Research and Development, ANID, through ANID-PIA Project AFB180004. MAC was financially supported by the Spanish Ministry of Science and Innovation through the Program Ramon y Cajal 2019, Grant RYC2019-026496-I. J.P.H.P. acknowledges the funding from the European Union's Horizon 2020 Marie Skłodowska-Curie Innovative Training Network (grant no. 675219) and Helmholtz Recruiting Initiative (award no. I-044-16-01). MPA was financially supported by the Junta de Andalucía through the Emergia Program 2020. Funding for open access charge: Universidad de Huelva / CBUA.

References

Acero, P., Ayora, C., Torrentó, C., Nieto, J.-M., 2006. The behavior of trace elements during schwertmannite precipitation and subsequent transformation into goethite and jarosite. Geochim. Cosmochim. Acta 70 (16), 4130–4139. https://doi.org/10.1016/j.gca.2006.06.1367.

Abdelmoula, M., Refait, P.h., Drissi, S.H., Mihe, J.P., Génin, J.-M.-R., 1996. Conversion electron Mössbauer spectroscopy and X-ray diffraction studies of the formation of carbonate-containing green rust one by corrosion of metallic iron in $NaHCO_3$ and ($NaHCO_3$ + NaCl) solutions. Corros. Sci. 38 (4), 623–633. https://doi.org/10.1016/0010-938X(95)00153-B.

Abramov, S.M., Tejada, J., Grimm, L., Schädler, F., Bulaev, A., Tomaszewski, E.J., Byrne, J.M., Straub, D., Thorwarth, H., Amils, R., Kleindienst, S., Kappler, A., 2020. Role of biogenic Fe(III) minerals as a sink and carrier of heavy metals in the Rio Tinto. Spain. Sci. Total Environ. 718, 137294. https://doi.org/10.1016/j.scitotenv.2020.137294.

Adachi, K., Oshima, N., Ohata, S., Yoshida, A., Moteki, N., Koike, M., 2021. Compositions and mixing states of aerosol particles by aircraft observations in the Arctic springtime, 2018. Atmos. Chem. Phys. 21 (5), 3607–3626. https://doi.org/10.5194/acp-21-3607-202110.5194/acp-21-3607-2021-supplement.

Ahmed, I.A.M., Benning, L.G., Kakonyi, G., Sumoondur, A.D., Terrill, N.J., Shaw, S., 2010. Formation of green rust sulfate: A combined in situ time-resolved X-ray scattering and electrochemical study. Langmuir 26 (9), 6593–6603. https://doi.org/10.1021/la903935j.

Aissa, R., Francois, M., Ruby, C., Fauth, F., Medjahdi, G., Abdelmoula, M., Genin, J.M., 2006. Formation and crystallographical structure of hydroxysulphate and hydroxycarbonate green rusts synthesized by coprecipitation. J. Phys. Chem. Solids 67, 1016–1019. https://doi.org/10.1016/j.jpcs.2006.01.020.

Anawar, H.Md, 2015. Sustainable Rehabilitation of Mining Waste and Acid Mine Drainage Using Geochemistry, Mine Type, Mineralogy, Texture, Ore Extraction and Climate Knowledge. J. Environ. Manag. 158.

Andujar, J.M., Aroba, J., de Torre, M.L.l., Grande, J.A., 2006. Contrast of evolution models for agricultural contaminants in ground waters by means of fuzzy logic and data mining. Environ. Geol. 49 (3), 458–466.

Antelo, J., Fiol, S., Gondar, D., Pérez, C., López, R., Arce, F., 2013. Cu(II) incorporation to schwertmannite: Effect on stability and reactivity under AMD conditions. Geochim. Cosmochim. Acta 119, 149–163. https://doi.org/10.1016/j.gca.2013.05.029.

Arden, T.V., 1950. The solubility products of ferrous and ferrosic hydroxides. J. Chem. Soc. 882–885. https://doi.org/10.1039/JR9500000882.

Asta, M.P., Ayora, C., Acero, P., Cama, J., 2010a. Field rates for natural attenuation of arsenic in Tinto Santa Rosa acid mine drainage (SW Spain). J. Hazard. Mater. 177 (1-3), 1102–1111. https://doi.org/10.1016/j.jhazmat.2010.01.034.

Asta, M.P., Ayora, C., Román-Ross, G., Cama, J., Acero, P., Gault, A.G., Charnock, J.M., Bardelli, F., 2010b. Natural attenuation of arsenic in the Tinto Santa Rosa acid stream (Iberian Pyritic Belt, SW Spain): The role of iron precipitates. Chem. Geol. 271 (1-2), 1–12. https://doi.org/10.1016/j.chemgeo.2009.12.005.

Asta, M.P., Calleja, M.L., Pérez-López, R., Auqué, L.F., 2015. Major hydrogeochemical processes in an Acid Mine Drainage affected estuary. Marine Poll. Bull. 91 (1), 295–305. https://doi.org/10.1016/j.marpolbul.2014.11.023.

Aumont, O., Bopp, L., 2006. Globalizing results from ocean in situ iron fertilization studies. Global Biogeochem. Cycles 20 (2), n/a–n/a. https://doi.org/10.1029/2005GB002591.

Ayala-Luis, K.B., Kaldor, D.K., Bender Koch, C., Strobel, B.W., Hansen, H.C.B., 2007. Synthesis of linear alkylbenzene sulphonate intercalated iron(II) iron(III) hydroxide sulphate (green rust) and adsorption of carbon tetrachloride. Clay Miner. 42 (3), 307–317. https://doi.org/10.1180/claymin.2007.042.3.04.

Ayala-Luis, K.B., Koch, C.B., Hansen, H.C.B., 2010a. Intercalation of linear C9–C16 carboxylates in layered FeII–FeIII-hydroxides (green rust) via ion exchange. Appl. Clay Sci. 48 (3), 334–341. https://doi.org/10.1016/j.clay.2010.01.003.

Ayala-Luis, K.B., Koch, C.B., Hansen, H.C.B., 2010b. One-pot synthesis and characterization of FeII–FeIII hydroxide (green rust) intercalated with C9–C14 linear alkyl carboxylates. Appl. Clay Sci. 50 (4), 512–519. https://doi.org/10.1016/j.clay.2010.10.002.

Ayora, C., Caraballo, M.A., Macias, F., Rötting, T.S., Carrera, J., Nieto, J.-M., 2013. Acid mine drainage in the Iberian Pyrite Belt: 2. Lessons learned from recent passive remediation experiences. Environ. Sci. Pollut. Control Ser. 20 (11), 7837–7853.

Ayora, C., Macías, F., Torres, E., Lozano, A., Carrero, S., Nieto, J.-M., Pérez-López, R., Fernández-Martínez, A., Castillo-Michel, H., 2016. Recovery of rare earth elements and yttrium from passive remediation systems of acid mine drainage. Environ. Sci. Technol. 50 (15), 8255–8262. https://doi.org/10.1021/acs.est.6b0208410.1021/acs.est.6b02084.s001.

Baes, C.F., Mesmer, R.S., 1976. The Hydrolysis of Cations. John Wiley & Sons, New York, London, Sydney, Toronto 1976 (489 Seiten, Preis: £ 18.60. Berichte der Bunsengesellschaft für Phys. Chemie 81, 245–246. https://doi.org/10.1002/bbpc.19770810252).

Barba-Brioso, C., Quaranta, G., Galán, E., Fernández-Caliani, J.C., Miras, A., 2010. The life cycle impact assessment applied to the Domingo Rubio tidal system by the study of seasonal variations of the aquatic eutrophication potential. Sci. of the Total Environ. 408 (23), 5897–5902.

Barge, L.M., Flores, E., Baum, M.M., VanderVelde, D.G., Russell, M.J., 2019. Redox and pH gradients drive amino acid synthesis in iron oxyhydroxide mineral systems. Proc. Natl. Acad. Sci. 116 (11), 4828–4833. https://doi.org/10.1073/pnas.1812098116.

Barham, R.J., Box, P.O., Aubrey, G., York, N., 1997. ligand , transforms to jarosites, hematites , and/or basic iron sulfate 12, 2751–2758.

Bhatia, M.P., Kujawinski, E.B., Das, S.B., Breier, C.F., Henderson, P.B., Charette, M.A., 2013. Greenland meltwater as a significant and potentially bioavailable source of iron to the ocean. Nature Geosci. 6 (4), 274–278. https://doi.org/10.1038/ngeo1746.

Bearcock, J.M., Perkins, W.T., Pearce, N.J.G., 2011. Laboratory studies using naturally occurring green rust to aid metal mine water remediation. J. Hazard. Mater. 190 (1-3), 466–473.

Beck, P., Pommerol, A., Zanda, B., Remusat, L., Lorand, J.P., Göpel, C., Hewins, R., Pont, S., Lewin, E., Quirico, E., Schmitt, B., Montes-Hernandez, G., Garenne, A., Bonal, L., Proux, O., Hazemann, J.L., Chevrier, V.F., 2015. A Noachian source region for the "Black Beauty" meteorite, and a source lithology for Mars surface hydrated dust? Earth Planet. Sci. Lett. 427, 104–111. https://doi.org/10.1016/j.epsl.2015.06.033.

Bekker, A., Slack, J.F., Planavsky, N., Krapez, B., Hofmann, A., Konhauser, K.O., Rouxel, O.J., 2010. Iron Formation: The Sedimentary Product of a Complex Interplay among Mantle, Tectonic, Oceanic, and Biospheric Processes. Econ. Geol. 105 (3), 467–508. https://doi.org/10.2113/gsecongeo.105.3.467.

Bekker, A., Planavsky, N.J., Krapež, B., Rasmussen, B., Hofmann, A., Slack, J.F., Rouxel, O.J., Konhauser, K.O., 2014. 9.18 - Iron Formations: Their Origins and Implications for Ancient Seawater Chemistry. In: Holland, H.D., Turekian, K.K. (Eds.), Treatise on Geochemistry (Second Edition). Elsevier, Oxford, pp. 561–628.

Benali, O., Abdelmoula, M., Refait, P., Génin, J.-M., 2001. Effect of orthophosphate on the oxidation products of Fe(II)-Fe(III) hydroxycarbonate: The transformation of green rust to ferrihydrite. Geochim. Cosmochim. Acta 65 (11), 1715–1726. https://doi.org/10.1016/S0016-7037(01)00556-7.

Bernal, J.D., Dasgupta, D.R., Mackay, A.L., 1959. The oxides and hydroxides of iron and their structural inter-relationships. Clay Miner. Bull. 4, 15–30. https://doi.org/10.1180/claymin.1959.004.21.02.

Berthelin, J., Ona-Nguema, G., Stemmler, S., Quantin, C., Abdelmoula, M., Jorand, F., 2006. Bioreduction of ferric species and biogenesis of green rusts in soils. Comptes Rendus Geosci. 338 (6–7), 447–455. https://doi.org/10.1016/j.crte.2006.04.013.

Bibring, J.-P., Arvidson, R.E., Gendrin, A., Gondet, B., Langevin, Y., Le Mouelic, S., Mangold, N., Morris, R.V., Mustard, J.F., Poulet, F., Quantin, C., Sotin, C., 2007. Coupled ferric oxides and sulfates on the Martian surface. Science 317 (5842), 1206–1210.

Biedermann, G., Schindler, P., 1957. On the solubility products of precipitated iron (III) hydroxide. Acta Chem. Scand. 11, 731–740.

Bigham, J.M., Carlson, L., Murad, E., 1994. Schwertmannite, a new iron oxyhydroxysulphate from Pyhäsalmi, Finland, and other localities. Mineral. Mag. 58 (393), 641–648. https://doi.org/10.1180/minmag.1994.058.393.14.

Bigham, J.M., Nordstrom, D.K., 2000. Iron and aluminum hydroxysulfates from acid sulfate waters. Rev. Miner. Geochem. 40 (1), 351–403. https://doi.org/10.2138/rmg.2000.40.7.

Bigham, J.M., Schwertmann, U., Carlson, L., Murad, E., 1990. A poorly crystallized oxyhydroxysulfate of iron formed by bacterial oxidation of Fe (II) in acid mine waters. Geochim. Cosmochim. Acta 54 (10), 2743–2758.

Bigham, J.M., Schwertmann, U., Traina, S.J., Winland, R.L., Wolf, M., 1996. Schwertmannite and the chemical modeling of iron in acid sulfate waters. Geochim. Cosmochim. Acta 60 (12), 2111–2121. https://doi.org/10.1016/0016-7037(96)00091-9.

Bishop, J.L., Pieters, C., Burns, R.G., 1993. Reflectance and Mössbauer spectroscopy of ferrihydrite-montmorillonite assemblages as Mars soil analog materials. Geochim. Cosmochim. Acta 57, 4583–4595. https://doi.org/10.1016/0016-7037(93)90184-X.

Bjerrum, C.J., Canfield, D.E., 2002. Ocean productivity before about 1.9 Gyr ago limited by phosphorus adsorption onto iron oxides. Nature 417 (6885), 159–162. https://doi.org/10.1038/417159a.

Blodau, C., 2004. Evidence for a hydrologically controlled iron cycle in acidic and iron rich sediments. Aquat. Sci. 66, 47–59. https://doi.org/10.1007/s00027-003-0689-y.

Blodau, C., 2006. A review of acidity generation and consumption in acidic coal mine lakes and their watersheds. Sci. Total Environ. 369, 307–332. https://doi.org/10.1016/j.scitotenv.2006.05.004.

Blodau, C., Gatzek, C., 2006. Chemical controls on iron reduction in schwertmannite-rich sediments. Chem. Geol. 235 (3-4), 366–376. https://doi.org/10.1016/j.chemgeo.2006.08.003.

Blowes, D.W., Ptacek, C.J., Jambor, J.L., Weisener, C.G., 2003. The Geochemistry of Acid Mine Drainage. In: Holland, Heinrich D., Turekian, Karl K. (Eds.), Treatise on Geochemistry, Pergamon, pp. 149–204. https://doi.org/10.1016/B0-08-043751-6/09137-4.

Bocher, F., Géhin, A., Ruby, C., Ghanbaja, J., Abdelmoula, M., Génin, J.-M., 2004. Coprecipitation of Fe(II-III) hydroxycarbonate green rust stabilised by phosphate adsorption. Solid State Sci. 6 (1), 117–124. https://doi.org/10.1016/j.solidstatesciences.2003.10.004.

Boyd, P.W., Ellwood, M.J., 2010. The biogeochemical cycle of iron in the ocean. Nature Geosci. 3 (10), 675–682. https://doi.org/10.1038/ngeo964.

Boily, J.-F., Gassman, P.L., Peretyazhko, T., Szanyi, J., Zachara, J.M., 2010. FTIR Spectral Components of Schwertmannite. Environ. Sci. Technol. 44 (4), 1185–1190. https://doi.org/10.1021/es902803u.

Bokare, A.D., Choi, W., 2014. Review of iron-free Fenton-like systems for activating H2O2 in advanced oxidation processes. J. Hazard. Mater. 275, 121–135.

Boland, D.D., Collins, R.N., Miller, C.J., Glover, C.J., Waite, T.D., 2014. Effect of solution and solid-phase conditions on the Fe(II)-accelerated transformation of ferrihydrite to lepidocrocite and goethite. Environ. Sci. Technol. 48 (10), 5477–5485. https://doi.org/10.1021/es4043275.

Bowles, J.F.W., 2021. Hydroxides. In: Alderton, David, Elias, Scott A. (Eds.). Encyclopedia of Geology, second ed. Academic Press, pp. 442–451. https://doi.org/10.1016/b978-0-08-102908-4.00162-4.

Brady, K.S., Bigham, J.M., Jaynes, W.F., Logan, T.J., 1986. Influence of sulfate on Fe-oxide formation comparisons with a stream receiving acid mine drainage. Clays Clay Miner. 3, 266–274.

Brearley, A.J., 1997. Phyllosilicates in the matrix of the unique carbonaceous chondrite Lewis Cliff 85332 and possible implications for the aqueous alteration of CI chondrites. Meteorit. Planet. Sci. 32, 377–388. https://doi.org/10.1111/j.1945-5100.1997.tb01281.x.

Brearley, A.J., 1989. Nature and origin of matrix in the unique type 3 chondrite. Kakangari. Geochim. Cosmochim. Acta 53, 2395–2411. https://doi.org/10.1016/0016-7037(89)90361-X.

Burton, E.D., Bush, R.T., Johnston, S.G., Watling, K.M., Hocking, R.K., Sullivan, L.A., Parker, G.K., 2009. Sorption of Arsenic(V) and Arsenic(III) to Schwertmannite. Environ. Sci. Technol. 43 (24), 9202–9207. https://doi.org/10.1021/es902461x.

Burton, E.D., Bush, R.T., Sullivan, L.A., 2006. Sedimentary iron geochemistry in acidic waterways associated with coastal lowland acid sulfate soils. Geochim. Cosmochim. Acta 70 (22), 5455–5468. https://doi.org/10.1016/j.gca.2006.08.016.

Burton, E.D., Bush, R.T., Sullivan, L.A., Mitchell, D.R.G., 2007. Reductive transformation of iron and sulfur in schwertmannite-rich accumulations associated with acidified coastal lowlands. Geochim. Cosmochim. Acta 71 (18), 4456–4473. https://doi.org/10.1016/j.gca.2007.07.007.

Caraballo, M.A., Michel, F.M., Hochella, M.F., 2015. The rapid expansion of environmental mineralogy in unconventional ways : Beyond the accepted definition of a mineral, the latest technology, and using nature as our guide. Am. Mineral. 100, 14–25.

Caraballo, M.A., Rimstidt, J.D., Macías, F., Nieto, J.M., Hochella, M.F., 2013. Metastability, nanocrystallinity and pseudo-solid solution effects on the understanding of schwertmannite solubility. Chem. Geol. 360-361, 22–31. https://doi.org/10.1016/j.chemgeo.2013.09.023.

Caraballo, M.A., Rötting, T.S., Nieto, J.M., Ayora, C., 2009. Sequential extraction and DXRD applicability to poorly crystalline Fe- and Al-phase characterization from an acid mine water passive remediation system. Am. Mineral. 94, 1029–1038. https://doi.org/10.2138/am.2009.3137.

Carlson, D.F., Pasma, J., Jacobsen, M.E., Hansen, M.H., Thomsen, S., Lillethorup, J.P., Tirsgaard, F.S., Flytkjær, A., Melvad, C., Laufer, K., Lund-Hansen, L.C., Meire, L., Rysgaard, S., 2019. Retrieval of ice samples using the ice drone. Front. Earth Sci. 7, 287. https://doi.org/10.3389/feart.2019.00287.

Castendyk, D.N., Webster-Brown, J.G., 2007. Sensitivity analyses in pit lake prediction, Martha mine, New Zealand 2: Geochemistry, water–rock reactions, and surface adsorption. Chem. Geol. 244 (1-2), 56–73. https://doi.org/10.1016/j.chemgeo.2007.06.005.

Chappell, H.F., Thom, W., Bowron, D.T., Faria, N., Hasnip, P.J., Powell, J.J., 2017. Structure of naturally hydrated ferrihydrite revealed through neutron diffraction and first-principles modeling. Phys. Rev. Mater. 1, 1–8. https://doi.org/10.1103/PhysRevMaterials.1.036002.

Chen, C., Kukkadapu, R., Sparks, D.L., 2015. Influence of Coprecipitated Organic Matter on Fe2+(aq)-Catalyzed Transformation of Ferrihydrite: Implications for Carbon Dynamics. Environ. Sci. Technol. 49 (18), 10927–10936. https://doi.org/10.1021/acs.est.5b02448.

Choi, J., Batchelor, B., 2008. Nitrate reduction by fluoride green rust modified with copper. Chemosphere 70 (6), 1108–1116. https://doi.org/10.1016/j.chemosphere.2007.07.053.

Chi Fru, E., Hemmingsson, C., Holm, M., Chiu, B., Iñiguez, E., 2016. Arsenic-induced phosphate limitation under experimental Early Proterozoic oceanic conditions. Earth Planet. Sci. Lett. 434, 52–63. https://doi.org/10.1016/j.epsl.2015.11.009.

Chislock, M.F., Doster, E., Zitomer, R.A., Wilson, A.E., 2013. Eutrophication: Causes, Consequences, and Controls in Aquatic Ecosystems. Nature Educ. Knowl. 4 (4), 10.

Christiansen, B.C., Balic-Zunic, T., Dideriksen, K., Stipp, S.L.S., 2009a. Identification of green rust in groundwater. Environ. Sci. Technol. 43 (10), 3436–3441. https://doi.org/10.1021/es8011047.

Christiansen, B.C., Balic-Zunic, T., Petit, P.-O., Frandsen, C., Mørup, S., Geckeis, H., Katerinopoulou, A., Stipp, S.L.S., 2009b. Composition and structure of an iron-bearing, layered double hydroxide (LDH) - Green rust sodium sulphate. Geochim. Cosmochim. Acta 73 (12), 3579–3592. https://doi.org/10.1016/j.gca.2009.03.032.

Chukhrov, F.V., Zvyagin, B.B., Gorshkov, A.I., Yermilova, L.P., Rudnitskaya, E.S., 1971. The Towe-Bradley phase—A product of the supergene alteration of ores. Izv. Akad Nauk SSSR (Geol Ser.) 1, 3.

Chukhov, F.V., Zvyagin, B.B., Gorshkov, A.I., Yermilova, L.P., Balashova, V.V., 1974. Ferrihydrite. Int. Geol. Rev. 16 (10), 1131–1143. https://doi.org/10.1080/00206817409471766.

Chukhrov, F. V., Zvyagin, B.B., Ermilova, L.P., Gorshkov, A.I., 1972. New data on iron oxides in the weathering zone. In: Proceedings of the International Clay Conference, Madrid, Spain, pp. 397−404.

Chukhrov, F.V., Zvyagin, B.B., Gorshkov, A.I., Yermilova, L.P., Balashova, V.V., 1973. Ferrihydrite. Izv. Akad. Nauk. SSSR. Ser. Geol. 4, 23–33.

Collins, R.N., Jones, A.M., Waite, T.D., 2010. Schwertmannite stability in acidified coastal environments. Geochim. Cosmochim. Acta 74, 482–496. https://doi.org/10.1016/j.gca.2009.10.014.

Cornell, R.M., Giovanoli, R., 1987. Effect of manganese on the transformation of ferrihydrite into goethite and jacobsite in alkaline media. Clays Clay Miner. 35, 11–20. https://doi.org/10.1346/CCMN.1987.0350102.

Cornell, R.M., Giovanoli, R., Schindler, P.W., 1987. Effect of Silicate Species on the Transformation of Ferrihydrite into Goethite and Hematite in Alkaline Media. Clays Clay Miner. 35, 21–28. https://doi.org/10.1346/CCMN.1987.0350103.

Cornell, R.M., Giovanoli, R., Schneider, W., 1989a. Review of the hydrolysis of iron (III) and the crystallization of amorphous iron(III) hydroxide hydrate. J. Chem. Technol. Biotechnol. 46, 115–134. https://doi.org/10.1002/jctb.280460204.

Cornell, R.M., Schneider, W., 1989. Formation of goethite from ferrihydrite at physiological pH under the influence of cysteine. Polyhedron 8, 149–155. https://doi.org/10.1016/S0277-5387(00)86496-7.

Cornell, R.M., Schneider, W., Giovanoli, R., 1989b. Phase transformations in the ferrihydrite/cysteine system. Polyhedron 8 (23), 2829–2836. https://doi.org/10.1016/S0277-5387(00)80544-6.

Cornell, R.M., Schwertmann, U., 2003. The Iron Oxides: Structure, Properties, Reactions, Occurrences and Uses, second ed. Wiley-VCH, Weinheim, Germany.

Cornell, R.M., Schwertmann, U., 1979. Influence of Organic Anions on the Crystallization of Ferrihydrite. Clays Clay Miner. 27, 402–410. https://doi.org/10.1346/CCMN.1979.0270602.

Cruz-Hernández, P., Peréz-López, R., Nieto, J.M., 2017. Role of Arsenic During the Aging of Acid Mine Drainage Precipitates. Procedia Earth Planet. Sci. 17, 233–236. https://doi.org/10.1016/j.proeps.2016.12.079.

Cudennec, Y., Lecerf, A., 2006. The transformation of ferrihydrite into goethite or hematite, revisited. J. Solid State Chem. 179 (3), 716–722. https://doi.org/10.1016/j.jssc.2005.11.030.

Das, S., Hendry, M.J., Essilfie-Dughan, J., 2011a. Transformation of two-line ferrihydrite to goethite and hematite as a function of pH and temperature. Environ. Sci. Technol. 45 (1), 268–275. https://doi.org/10.1021/es101903y.

Das, S., Hendry, M.J., Essilfie-Dughan, J., 2011b. Effects of Adsorbed Arsenate on the Rate of Transformation of 2-Line Ferrihydrite at pH 10. Environ. Sci. Technol. 45 (13), 5557–5563. https://doi.org/10.1021/es200107m.

Davidson, L.E., Shaw, S., Benning, L.G., 2008. The kinetics and mechanisms of schwertmannite transformation to goethite and hematite under alkaline conditions. Am. Mineral. 93 (8-9), 1326–1337. https://doi.org/10.2138/am.2008.2761.

Dehouck, E., McLennan, S.M., Sklute, E.C., Dyar, M.D., 2017. Stability and fate of ferrihydrite during episodes of water/rock interactions on early Mars: An experimental approach. J. Geophys. Res. Planets 122, 358–382. https://doi.org/10.1002/2016JE005222.

Dekov, V.M., Vanlierde, E., Billström, K., Garbe-Schönberg, C.D., Weiss, D.J., Gatto Rotondo, G., Van Meel, K., Kuzmann, E., Fortin, D., Darchuk, L., Van Grieken, R., 2014. Ferrihydrite precipitation in groundwater-fed river systems (Nete and Demer river basins, Belgium): Insights from a combined Fe-Zn-Sr-Nd-Pb-isotope study. Chem. Geol. 386, 1–15. https://doi.org/10.1016/j.chemgeo.2014.07.023.

Delina, R.E., Arcilla, C., Otake, T., Garcia, J.J., Tan, M., Ito, A., 2020. Chromium occurrence in a nickel laterite profile and its implications to surrounding surface waters. Chem. Geol. 558, 119863. https://doi.org/10.1016/j.chemgeo.2020.119863.

Drissi, S.H., Refait, P.h., Abdelmoula, M., Génin, J.M.R., 1995. The Preparation and thermodynamic properties of Fe(II)-Fe(III) hydroxide-carbonate (Green-Rust-1) - Pourbaix diagram of iron in carbonate-containing aqueous-media. Corros. Sci. 37 (12), 2025–2041. https://doi.org/10.1016/0010-938X(95)00096-3.

Dodds, W.K., Bouska, W.W., Eitzmann, J.L., Pilger, T.J., Pitts, K.L., Riley, A.J., Schloesser, J.T., Thornbrugh, D.J., 2009. Eutrophication of U.S. freshwaters: analysis of potential economic damages. Environ. Sci. Technol. 43 (1), 12–19.

Dold, B., Gonzalez-Toril, E., Aguilera, A., Lopez-Pamo, E., Cisternas, M.E., Bucchi, F., Amils, R., 2013. Acid Rock Drainage and Rock Weathering in Antarctica: Important Sources for Iron Cycling in the Southern Ocean. Env. Sci. Tech. 47 (12), 6129–6136. https://doi.org/10.1021/es305141b.

Dold, B., Fontboté, L., 2002. A mineralogical and geochemical study of element mobility in sulfide mine tailings of Fe oxide Cu–Au deposits from the Punta del Cobre belt, northern Chile. Chem. Geol. 189 (3-4), 135–163. https://doi.org/10.1016/S0009-2541(02)00044-X.

Dore, E., Fancello, D., Rigonat, N., Medas, D., Cidu, R., Da Pelo, S., Frau, F., Lattanzi, P., Marras, P.A., Meneghini, C., Podda, F., Rimondi, V., Runkel, R.L., Kimball, B., Wanty, R.B., De Giudici, G., 2020. Natural attenuation can lead to environmental resilience in mine environment. Appl. Geochem. 117, 104597. https://doi.org/10.1016/j.apgeochem.2020.104597.

Duval, S., Baymann, F., Schoepp-Cothenet, B., Trolard, F., Bourrié, G., Grauby, O., Branscomb, E., Russell, M.J., Nitschke, W., 2019. Fougerite: the not so simple progenitor of the first cells. Interface Focus 9 (6), 20190063. https://doi.org/10.1098/rsfs.2019.0063.

Edraki, M., Baumgart, T., Manlapig, E., Bradshaw, D., Franks, D.M., Moran, C.J., 2014. Designing Mine Tailings for Better Environmental, Social and Economic Outcomes: A Review of Alternative Approaches. J. Clean. Prod. 84 (1), 411–420.

Eggleton, R.A., Fitzpatrick, R.W., 1988. New Data and a Revised Structural Model for Ferrihydrite. Clays Clay Miner. 36, 111–124. https://doi.org/10.1346/CCMN.1988.0360203.

Eickhoff, M., Obst, M., Schröder, C., Hitchcock, A.P., Tyliszczak, T., Martinez, R.E., Robbins, L.J., Konhauser, K.O., Kappler, A., 2014. Nickel partitioning in biogenic and abiogenic ferrihydrite: The influence of silica and implications for ancient environments. Geochim. Cosmochim. Acta 140, 65–79. https://doi.org/10.1016/j.gca.2014.05.021.

Falagán, C., Grail, B.M., Johnson, D.B., 2017. New Approaches for Extracting and Recovering Metals from Mine Tailings. Minerals Eng. 106, 71–78.

Farrand, W.H., Glotch, T.D., Rice, J.W., Hurowitz, J.A., Swayze, G.A., 2009. Discovery of jarosite within the Mawrth Vallis region ofMars: implications for the geologic history of the region. Icarus 204 (2), 478–488.

Fei, Y., Hua, J., Liu, C., Li, F., Zhu, Z., Xiao, T., Chen, M., Gao, T., Wei, Z., Hao, L., 2018. Aqueous Fe(II)-Induced Phase Transformation of Ferrihydrite Coupled Adsorption/Immobilization of Rare Earth Elements. Minerals 8, 357. https://doi.org/10.3390/min8080357.

Feitknecht, W., Keller, G., 1950. Über Die dunkelgrünen Hydroxyverbindungen des Eisens. Zeitschrift für anorganische Chemie 262 (1-5), 61–68. https://doi.org/10.1002/zaac.19502620110.

Feng, X., Wang, X., Zhu, M., Koopal, L.K., Xu, H., Wang, Y., Liu, F., 2015. Effects of phosphate and silicate on the transformation of hydroxycarbonate green rust to ferric oxyhydroxides. Geochim. Cosmochim. Acta 171, 1–14. https://doi.org/10.1016/j.gca.2015.08.020.

Fernandez-Martinez, A., Timon, V., Roman-Ross, G., Cuello, G.J., Daniels, J.E., Ayora, C., 2010. The structure of schwertmannite, a nanocrystalline iron oxyhydroxysulfate. Am. Mineral. 95 (8-9), 1312–1322. https://doi.org/10.2138/am.2010.3446.

Filip, J., Zboril, R., Schneeweiss, O., Zeman, J., Cernik, M., Kvapil, P., Otyepka, M., 2007. Environmental applications of chemically pure natural ferrihydrite. Environ. Sci. Tech. 41 (12), 4367–4374. https://doi.org/10.1021/es062312t10.1021/es062312t.s001.

Fitzpatrick, R., Raven, M., Self, P., Shand, P., Mosley, L., Simpson, S., Baker, A., 2012. Occurrence, genesis and environmental significance of schwertmannite in re-flooded Acid Sulfate Soils in the Lower Murray Reclaimed Irrigation Area. In: Proceedings Combined Australian Regolith Geoscientists Association and Australian Clay Minerals Society Conference: Mildura 7–10 February (2012), pp. 147–152.

Fleischer, M., Chao, G.Y., Kato, A., 1975. New Mineral Names. Am. Mineral. 60, 485–489. https://doi.org/10.2138/am-2015-nmn1005-616.

Fox, L.E., 1988. The solubility of colloidal ferric hydroxide and its relevance to iron concentrations in river water. Geochim. Cosmochim. Acta 52 (3), 771–777. https://doi.org/10.1016/0016-7037(88)90337-7.

French, R.A., Caraballo, M.A., Kim, B., Rimstidt, J.D., Murayama, M., Hochella, M.F., 2012. The enigmatic iron oxyhydroxylsulfate nanomineral schwertmannite: morphology, structure and composition. Am. Miner. 97, 1469–1482.

Fukushi, K., Sasaki, M., Sato, T., Yanase, N., Amano, H., Ikeda, H., 2003. A natural attenuation of arsenic in drainage from an abandoned arsenic mine dump. Appl. Geochem. 18, 1267–1278. https://doi.org/10.1016/S0883-2927(03)00011-8.

Funnell, N.P., Fulford, M.F., Inoué, S., Kletetschka, K., Michel, F.M., Goodwin, A.L., 2020. Nanocomposite structure of two-line ferrihydrite powder from total scattering. Commun. Chem. 3 (1). https://doi.org/10.1038/s42004-020-0269-2.

Gagliano, W.B., Brill, M.R., Bigham, J.M., Jones, F.S., Traina, S.J., 2004. Chemistry and mineralogy of ochreous sediments in a constructed mine drainage wetland. Geochim. Cosmochim. Acta 68, 2119–2128. https://doi.org/10.1016/j.gca.2003.10.038.

Gálvez, N., Barrón, V., Torrent, J., 1999. Effect of phosphate on the crystallization of hematite, goethite, and lepidocrocite from ferrihydrite. Clays Clay Miner. 47, 304–311. https://doi.org/10.1346/CCMN.1999.0470306.

Géhin, A., Ruby, C., Abdelmoula, M., Benali, O., Ghanbaja, J., Refait, P., Génin, J.-M., 2002. Synthesis of Fe(II-III) hydroxysulphate green rust by coprecipitation. Solid State Sci. 4 (1), 61–66. https://doi.org/10.1016/S1293-2558(01)01219-5.

Génin, J.-M., Ruby, C., 2004. Anion and cation distributions in Fe(II–III) hydroxysalt green rusts from XRD and Mössbauer analysis (carbonate, chloride, sulphate,); the "fougerite" mineral. Solid State Sci. 6 (7), 705–718. https://doi.org/10.1016/j.solidstatesciences.2004.03.021.

Génin, J.-M., Aïssa, R., Géhin, A., Abdelmoula, M., Benali, O., Ernstsen, V., Ona-Nguema, G., Upadhyay, C., Ruby, C., 2005. Fougerite and FeII–III hydroxycarbonate green rust; ordering, deprotonation and/or cation substitution; structure of hydrotalcite-like compounds and mythic ferrosic hydroxide. Solid State Sci. 7 (5), 545–572. https://doi.org/10.1016/j.solidstatesciences.2005.02.001.

Génin, J.-M., Ruby, C., Upadhyay, C., 2006. Structure and thermodynamics of ferrous, stoichiometric and ferric oxyhydroxycarbonate green rusts; redox flexibility and fougerite mineral. Solid State Sci. 8 (11), 1330–1343. https://doi.org/10.1016/j.solidstatesciences.2006.05.010.

Génin, J.-M.- R., Ruby, C., 2008. Structure of some FeII – III hydroxysalt green rusts (carbonate, oxalate, methanoate) from Mössbauer spectroscopy. Hyperfine Interact. 185 (1-3), 191–196. https://doi.org/10.1007/s10751-008-9827-1.

Gilbert, B., Erbs, J.J., Penn, R.L., Petkov, V., Spagnoli, D., Waychunas, G.A., 2013. A disordered nanoparticle model for 6-line ferrihydrite. Am. Mineral. 98 (8-9), 1465–1476. https://doi.org/10.2138/am.2013.4421.

Girard, A., Chaudron, G., 1935. Sur la constitution de la rouille. C. R. Acad. Sci. 200, 127–129.

Gavrilescu, M., Demnerová, K., Aamand, J., Agathos, S., Fava, F., 2015. Emerging pollutants in the environment: present and future challenges in biomonitoring, ecological risks and bioremediation. Nat. Biotechnol. 32 (1), 147–156.

Greshake, A., 1997. The primitive matrix components of the unique carbonaceous chondrite Acfer 094: A TEM study. Geochim. Cosmochim. Acta 61 (2), 437–452. https://doi.org/10.1016/S0016-7037(96)00332-8.

Guyodo, Y., Banerjee, S.K., Lee Penn, R., Burleson, D., Berquo, T.S., Seda, T., Solheid, P., 2006. Magnetic properties of synthetic six-line ferrihydrite nanoparticles. Phys. Earth Planet. Inter. 154 (3-4), 222–233. https://doi.org/10.1016/j.pepi.2005.05.009.

Halevy, I., Alesker, M., Schuster, E.M., Popovitz-Biro, R., Feldman, Y., 2017. A key role for green rust in the Precambrian oceans and the genesis of iron formations. Nat. Geosci. 10 (2), 135–139. https://doi.org/10.1038/ngeo2878.

Hamilton, D.S., Moore, J.K., Arneth, A., Bond, T.C., Carslaw, K.S., Hantson, S., Ito, A., Kaplan, J.O., Lindsay, K., Nieradzik, L., Rathod, S.D., Scanza, R.A., Mahowald, N.M., 2020. Impact of Changes to the Atmospheric Soluble Iron Deposition Flux on Ocean Biogeochemical Cycles in the Anthropocene. Global Biogeochem. Cycles 34 (3). https://doi.org/10.1029/2019GB006448.

Hanna, K., Kone, T., Ruby, C., 2010. Fenton-like oxidation and mineralization of phenol using synthetic Fe(II)–Fe(III) green rusts. Environ. Sci. Pollut. Res. 17 (1), 124–134. https://doi.org/10.1007/s11356-009-0148-y.

Hansel, C.M., Benner, S.G., Fendorf, S., 2005. Competing Fe (II)-Induced Mineralization Pathways of Ferrihydrite. Environ. Sci. Technol. 39 (18), 7147–7153. https://doi.org/10.1021/es050666z10.1021/es050666z.s001.

Hansen, H.C.B., Poulsen, I.F., 1999. Interaction of synthetic sulphate "Green rust" with phosphate and the crystallization of vivianite. Clays Clay. Miner. 47, 312–318. https://doi.org/10.1346/Ccmn.1999.0470307.

Harrington, R., Hausner, D.B., Xu, W., Bhandari, N., Michel, F.M., Brown, G.E., Strongin, D.R., Parise, J.B., 2011. Neutron pair distribution function study of two-line ferrihydrite. Environ. Sci. Technol. 45 (23), 9883–9890. https://doi.org/10.1021/es2020633.

Harrison, P.M., Fischbach, F.A., Hoy, T.G., Haggis, G.H., 1967. Ferric Oxyhydroxide Core of Ferritin. Nature 216 (5121), 1188–1190. https://doi.org/10.1038/2161188a0.

Hassellöv, M., von der Kammer, F., 2008. Iron oxides as geochemical nanovectors for metal transport in soil–river systems. Elements 4 (6), 401–406. https://doi.org/10.2113/gselements.4.6.401.

Hawkings, J.R., Benning, L.G., Raiswell, R., Kaulich, B., Araki, T., Abyaneh, M., Stockdale, A., Koch-Müller, M., Wadham, J.L., Tranter, M., 2018. Biolabile ferrous iron bearing nanoparticles in glacial sediments. Earth Planet. Sci. Lett. 493, 92–101. https://doi.org/10.1016/j.epsl.2018.04.022.

Hawkings, J., Wadham, J., Tranter, M., Raiswell, R., Benning, L.G., Statham, P.J., Tedstone, A., Nienow, P., Lee, K., Telling, J., 2014. Ice sheets as a significant source of highly reactive nanoparticulate iron to the oceans. Nat. Commun. 5, 3929. https://doi.org/10.1038/ncomms4929.

Heald, S.M., Stern, E.A., Bunker, B., Holt, E.M., Holt, S.L., 1979. Structure of the iron-containing core in ferritin by the extended x-ray absorption fine structure technique. J. Am. Chem. Soc. 101 (1), 67–73. https://doi.org/10.1021/ja00495a012.

Hiemstra, T., 2015. Formation, stability, and solubility of metal oxide nanoparticles: Surface entropy, enthalpy, and free energy of ferrihydrite. Geochim. Cosmochim. Acta 158, 179–198. https://doi.org/10.1016/j.gca.2015.02.032.

Hiemstra, T., 2013. Surface and mineral structure of ferrihydrite. Geochim. Cosmochim. Acta 105, 316–325. https://doi.org/10.1016/j.gca.2012.12.002.

Hochella, M.F., Lower, S.K., Maurice, P.A., Penn, R.L., Sahai, N., Sparks, D.L., Twining, B.S., 2008. Nanominerals, Mineral Nanoparticles, and Earth Systems. Science (80-.) 319 (5870), 1631–1635.

Huang, L.-Z., Ayala-Luis, K.B., Fang, L., Dalby, K.N., Kasama, T., Bender Koch, C., Hansen, H.C.B., 2013. Oxidation of Dodecanoate Intercalated Iron(II)–Iron(III) Layered Double Hydroxide to Form 2D Iron(III) (Hydr)oxide Layers. Eur. J. Inorg. Chem. 2013 (33), 5718–5727. https://doi.org/10.1002/ejic.v2013.3310.1002/ejic.201300735.

Huminicki, D.M.C., Hawthorne, F.C., 2003. The crystal structure of nickischerite, NaFe2+Al3(SO4)2(OH)18(H2O)12, a mineral of the shigaite group. Can. Miner. 41, 79–82. https://doi.org/10.2113/gscanmin.41.1.79.

Hurowitz, J.A., Fischer, W.W., Tosca, N.J., Milliken, R.E., 2010. Origin of acidic surface waters and the evolution of atmospheric chemistry on early Mars. Nature Geosci. 3, 323–326.

Jambor, J.L., Dutrizac, J.E., 1998. Occurrence and Constitution of Natural and Synthetic Ferrihydrite, a Widespread Iron Oxyhydroxide. Chem. Rev. 98 (7), 2549–2586. https://doi.org/10.1021/cr970105t.

Janney, D.E., Cowley, J.M., Buseck, P.R., 2001. Structure of synthetic 6-line ferrihydrite by electron nanodiffraction. Am. Mineral. 86 (3), 327–335. https://doi.org/10.2138/am-2001-2-316.

Janney, D.E., Cowley, J.M., Buseck, P.R., 2000. Structure of synthetic 2-line ferrihydrite by electron nanodiffraction. Am. Mineral. 85 (9), 1180–1187. https://doi.org/10.2138/am-2000-8-910.

Jansen, E., Kyek, A., Schafer, W., Schwertmann, U., 2002. The structure of six-line ferrihydrite. Appl. Phys. A 74, S1004–S1006.

Johnson, C.A., Freyer, G., Fabisch, M., Caraballo, M.A., Küsel, K., Hochella Jr., M.F., 2014. Observations and assessment of iron oxide and green rust nanoparticles in metal-polluted mine drainage within a steep redox gradient. Environ. Chem. 11, 377–391.

Johnson, J.E., Muhling, J.R., Cosmidis, J., Rasmussen, B., Templeton, A.S., 2018. Low-Fe(III) Greenalite Was a Primary Mineral From Neoarchean Oceans. Geophys. Res. Lett. 45 (7), 3182–3192. https://doi.org/10.1002/grl.v45.710.1002/2017GL076311.

Johnson, C.A., Murayama, M., Küsel, K., Hochella, M.F., 2015. Polycrystallinity of green rust minerals and their synthetic analogs: Implications for particle formation and reactivity in complex systems. Am. Mineral. 100 (10), 2091–2105.

Johnston, J.H., Lewis, D.G., 1983. A detailed study of the transformation of ferrihydrite to hematite in an aqueous medium at 92°C. Geochim. Cosmochim. Acta 47 (11), 1823–1831. https://doi.org/10.1016/0016-7037(83)90200-4.

Jolivet, J.-P., Tronc, E., Chanéac, C., 2006. Iron oxides: From molecular clusters to solid. A nice example of chemical versatility. Comptes Rendus - Geosci. 338 (6-7), 488–497. https://doi.org/10.1016/j.crte.2006.04.014.

Jones, C., Nomosatryo, S., Crowe, S.A., Bjerrum, C.J., Canfield, D.E., 2015. Iron oxides, divalent cations, silica, and the early earth phosphorus crisis. Geology 43, 135–138. https://doi.org/10.1130/G36044.1.

Jönsson, J., Persson, P., Sjöberg, S., Lövgren, L., 2005. Schwertmannite precipitated from acid mine drainage: Phase transformation, sulphate release and surface properties. Appl. Geochemistry 20 (1), 179–191. https://doi.org/10.1016/j.apgeochem.2004.04.008.

Jönsson, J., Jönsson, J., Lövgren, L., 2006. Precipitation of secondary Fe(III) minerals from acid mine drainage. Appl. Geochem. 21, 437–445. https://doi.org/10.1016/j.apgeochem.2005.12.008.

Jorand, F., Zegeye, A., Ghanbaja, J., Abdelmoula, M., 2011. The formation of green rust induced by tropical river biofilm components. Sci. Total Environ. 409 (13), 2586–2596. https://doi.org/10.1016/j.scitotenv.2011.03.030.

Jørgensen, B.B., Laufer, K., Michaud, A.B., Wehrmann, L.M., 2021. Biogeochemistry and microbiology of high Arctic marine sediment ecosystems—Case study of Svalbard fjords. Limnol. Oceanogr. 66, S273–S292. https://doi.org/10.1002/lno.11551.

Kantar, C., Oral, O., Urken, O., Oz, N.A., Keskin, S., 2019. Oxidative degradation of chlorophenolic compounds with pyrite-Fenton process. Env. Pollut. 247, 349–361.

Kappler, A., Pasquero, C., Konhauser, K.O., Newman, D.K., 2005. Deposition of banded iron formations by anoxygenic phototrophic Fe(II)-oxidizing bacteria. Geology 33 (11), 865. https://doi.org/10.1130/G21658.110.1130/2005170.

Karimian, I., Johnston, S.G., Burton, E.D., 2018. Iron and sulfur cycling in acid sulfate soil wetlands under dynamic redox conditions: A review. Chemosphere 197, 803–816. https://doi.org/10.1016/j.chemosphere.2018.01.096.

Kawamoto, K., Yokoo, H., Ochiai, A., Nakano, Y., Takeda, A., Oki, T., Takehara, M., Uehara, M., Fukuyama, K., Ohara, Y., Ohnuki, T., Hochella, M.F., Utsunomiya, S., 2021. The role of nanoscale aggregation of ferrihydrite and amorphous silica in the natural attenuation of contaminant metals at mill tailings sites. Geochim. et Cosmochim. Acta 298, 207–226. https://doi.org/10.1016/j.gca.2021.02.004.

Kawano, M., Tomita, K., 2001. Geochemical modeling of bacterially induced mineralization of schwertmannite and jarosite in sulfuric acid spring water. Am. Mineral. 86 (10), 1156–1165. https://doi.org/10.2138/am-2001-1005.

Keller, L.P., Buseck, P.R., 1990. Matrix mineralogy of the Lancé CO3 carbonaceous chondrite: A transmission electron microscope study. Geochim. Cosmochim. Acta 54 (4), 1155–1163. https://doi.org/10.1016/0016-7037(90)90446-R.

Khamphila, K., Kodama, R., Sato, T., Otake, T., 2017. Adsorption and Post Adsorption Behavior of Schwertmannite with Various Oxyanions. J. Miner. Mater. Charact. Eng. 05 (02), 90–106. https://doi.org/10.4236/jmmce:2017.52008.

Klein, C., 2005. Some Precambrian banded iron-formations (BIFs) from around the world: Their age, geologic setting, mineralogy, metamorphism, geochemistry, and origins. Am. Mineral. 90 (10), 1473–1499. https://doi.org/10.2138/am.2005.1871.

Koeksoy, E., Sundman, A., Byrne, J.M., Lohmayer, R., Planer-Friedrich, B., Halevy, I., Konhauser, K.O., Kappler, A., 2019. Formation of green rust and elemental sulfur in an analogue for oxygenated ferro-euxinic transition zones of Precambrian oceans. Geology 47, 211–214. https://doi.org/10.1130/G45501.1.

Köhler, S.J., Lidman, F., Laudon, H., 2014. Landscape types and pH control organic matter mediated mobilization of Al, Fe, U and La in boreal catchments. Geochim. Cosmochim. Acta 135, 190–202. https://doi.org/10.1016/j.gca.2014.03.033.

Kone, T., Hanna, K., Abdelmoula, M., Ruby, C., Carteret, C., 2009. Reductive transformation and mineralization of an azo dye by hydroxysulphate green rust preceding oxidation using H2O2 at neutral pH. Chemosphere 75 (2), 212–219. https://doi.org/10.1016/j.chemosphere.2008.12.002.

Konhauser, K.O., Hamade, T., Raiswell, R., Morris, R.C., Ferris, F.G., Southam, G., Canfield, D.E., 2002. Could bacteria have formed the Precambrian banded iron formations? Geology 30, 1079–1082. https://doi.org/10.1130/0091-7613(2002)030%3C1079:CBHFTP%3E2.0.CO;2.

Koski, R.A., Munk, LeeAnn, Foster, A.L., Shanks, W.C., Stillings, L.L., 2008. Sulfide oxidation and distribution of metals near abandoned copper mines in coastal environments, Prince William Sound, Alaska, USA. Applied Geochem. 23 (2), 227–254. https://doi.org/10.1016/j.apgeochem.2007.10.007.

Knorr, K.-H., Blodau, C., 2007. Controls on schwertmannite transformation rates and products. Appl. Geochem. 22 (9), 2006–2015. https://doi.org/10.1016/j.apgeochem.2007.04.017.

Kwon, S.-K., Kimijima, K., Kanie, K., Suzuki, S., Muramatsu, A., Saito, M., Shinoda, K., Waseda, Y., 2007. Influence of silicate ions on the formation of goethite from green rust in aqueous solution. Corros. Sci. 49 (7), 2946–2961. https://doi.org/10.1016/j.corsci.2007.01.007.

Kumpulainen, S., Räisänen, M.-L., Von Der Kammer, F., Hofmann, T., 2008. Ageing of synthetic and natural schwertmannites at pH 2–8. Clay Miner. 43 (3), 437–448. https://doi.org/10.1180/claymin.2008.043.3.08.

Langmuir, D., Whittemore, D.O., 1971. Variations in the Stability of Precipitated Ferric Oxyhydroxides, in: Nonequilibrium Systems in Natural Water Chemistry, Advances in Chemistry. American Chemical Society, pp. 209-234 SE–8. https://doi.org/10.1021/ba-1971-0106.ch008.

Legrand, L., Abdelmoula, M., Géhin, A., Chaussé, A., Génin, J.-M.-R., 2001. Electrochemical formation of a new Fe(II)-Fe(III) hydroxy-carbonate green rust: characterisation and morphology. Electrochim. Acta 46 (12), 1815–1822. https://doi.org/10.1016/S0013-4686(00)00728-3.

Lenstra, W.K., Hermans, M., Séguret, M.J.M., Witbaard, R., Behrends, T., Dijkstra, N., van Helmond, N.A.G.M., Kraal, P., Laan, P., Rijkenberg, M.J.A., Severmann, S., Teacă, A., Slomp, C.P., 2019. The shelf-to-basin iron shuttle in the Black Sea revisited. Chemical Geol. 511, 314–341.

Li, Y., Yang, M., Pentrak, M., He, H., Arai, Y., 2020. Carbonate-Enhanced Transformation of Ferrihydrite to Hematite. Environ. Sci. Technol. 54 (21), 13701–13708. https://doi.org/10.1021/acs.est.0c0404310.1021/acs.est.0c04043.s001.

Liao, Y., Zhou, L., Bai, S., Liang, J., Wang, S., 2009. Occurrence of biogenic schwertmannite in sludge bioleaching environments and its adverse effect on solubilization of sludge-borne metals. Appl. Geochem. 24, 1739–1746. https://doi.org/10.1016/j.apgeochem.2009.05.003.

Lima, B.D., Teixeira, E.C., Hower, J.C., Civeira, M.S., Ramírez, O., Yang, C.-X., Oliveira, M.L.S., Silva, L.F.O., 2021. Metal-enriched nanoparticles and black carbon: A perspective from the Brazil railway system air pollution. Geosci. Front. 12 (3), 101129. https://doi.org/10.1016/j.gsf.2020.12.010.

Liu, Y., Goudge, T.A., Catalano, J.G., Wang, A., 2018. Spectral and stratigraphic mapping of hydrated minerals associated with interior layered deposits near the southern wall of Melas Chasma, Mars. Icarus 302, 62–79. https://doi.org/10.1016/j.icarus.2017.11.006.

Liu, Y., Jin, W., Zhao, Y., Zhang, G., Zhang, W., 2017. Enhanced catalytic degradation of methylene blue by alpha-Fe2O3/graphene oxide via heterogeneous photo-Fenton reactions. Appl. Catal. B. 206, 642–652.

Liu, C., Zhu, Z., Li, F., Liu, T., Liao, C., Lee, J.J., Shih, K., Tao, L., Wu, Y., 2016. Fe(II)-induced phase transformation of ferrihydrite: The inhibition effects and stabilization of divalent metal cations. Chem. Geol. 444, 110–119. https://doi.org/10.1016/j.chemgeo.2016.10.002.

Liu, H., Guo, H., Li, P., Wei, Y.u., 2008. The transformation of ferrihydrite in the presence of trace Fe(II): The effect of the anionic media. J. Solid State Chem. 181 (10), 2666–2671. https://doi.org/10.1016/j.jssc.2008.06.052.

Liu, H., Li, P., Zhu, M., Wei, Y., Sun, Y., 2007. Fe(II)-induced transformation from ferrihydrite to lepidocrocite and goethite. J. Solid State Chem. 180, 2121–2128. https://doi.org/10.1016/j.jssc.2007.03.022.

Liu, H., Ma, M., Qin, M., Yang, L., Wei, Y.u., 2010. Studies on the controllable transformation of ferrihydrite. J. Solid State Chem. 183 (9), 2045–2050. https://doi.org/10.1016/j.jssc.2010.07.012.

Loan, M., Cowley, J.M., Hart, R., Parkinson, G.M., 2004. Evidence on the structure of synthetic schwertmannite. Am. Miner. 89 (11-12), 1735–1742. https://doi.org/10.2138/am-2004-11-1220.

Lozano, A., Ayora, C., Fernández-Martínez, A., 2020. Sorption of rare earth elements on schwertmannite and their mobility in acid mine drainage treatments. Appl. Geochem. 113,. https://doi.org/10.1016/j.apgeochem.2019.104499 104499.

Macera, L., Taglieri, G., Daniele, V., Passacantando, M., Orazio, F.D., 2020. Nano-Sized Fe (III) Oxide Particles Starting from an Innovative and Eco-Friendly Synthesis Method.

Macrae, C.F., Bruno, I.J., Chisholm, J.A., Edgington, P.R., McCabe, P., Pidcock, E., Rodriguez-Monge, L., Taylor, R., van de Streek, J., Wood, P.A., 2008. Mercury CSD 2.0–new features for the visualization and investigation of crystal structures. J. Appl. Crystallogr. 41 (2), 466–470. https://doi.org/10.1107/S0021889807067908.

Maillot, F., Morin, G., Juillot, F., Bruneel, O., Casiot, C., Ona-Nguema, G., Wang, Y., Lebrun, S., Aubry, E., Vlaic, G., Brown, G.E., 2013. Structure and reactivity of As (III)- and As(V)-rich schwertmannites and amorphous ferric arsenate sulfate from the Carnoulès acid mine drainage, France: Comparison with biotic and abiotic model compounds and implications for As remediation. Geochim. Cosmochim. Acta 104, 310–329. https://doi.org/10.1016/j.gca.2012.11.016.

Maillot, F., Morin, G., Wang, Y., Bonnin, D., Ildefonse, P., Chaneac, C., Calas, G., 2011. New insight into the structure of nanocrystalline ferrihydrite: EXAFS evidence for tetrahedrally coordinated iron(III). Geochim. Cosmochim. Acta 75 (10), 2708–2720. https://doi.org/10.1016/j.gca.2011.03.011.

Majzlan, J., Navrotsky, A., Schwertmann, U., 2004. Thermodynamics of iron oxides: Part III. Enthalpies of formation and stability of ferrihydrite (∼Fe(OH)3), schwertmannite (∼FeO(OH)3/4(SO4)1/8), and ε-Fe2O3. Geochim. Cosmochim. Acta 68 (5), 1049–1059. https://doi.org/10.1016/S0016-7037(03)00371-5.

Manceau, A., 2019. Comment on "roles of Hydration and Magnetism on the Structure of Ferrihydrite from First Principles". ACS Earth Sp. Chem. 3 (8), 1576–1580. https://doi.org/10.1021/acsearthspacechem.9b00018.

Manceau, A., 2011. Critical evaluation of the revised akdalaite model for ferrihydrite. Am. Mineral. 96 (4), 521–533. https://doi.org/10.2138/am.2011.3583.

Manceau, A., 2009. Evaluation of the structural model for ferrihydrite derived from real-space modelling of high-energy X-ray diffraction data. Clay Miner. 44 (1), 19–34. https://doi.org/10.1180/claymin.2009.044.1.19.

Manceau, A., Drits, V.A., 1993. Local Structure of Ferrihydrite and Feroxyhite by EXAFS Spectroscopy. Clay Miner. 28 (2), 165–184. https://doi.org/10.1180/claymin.1993.028.2.01.

Manceau, A., Gates, W.P., 1997. Surface structural model for ferrihydrite. Clays Clay Miner. 45, 448–460. https://doi.org/10.1346/CCMN.1997.0450314.

Manceau, A., Skanthakumar, S., Soderholm, L., 2014. PDF analysis of ferrihydrite: Critical assessment of the under-constrained akdalaite model. Am. Mineral. 99, 102–108. https://doi.org/10.2138/am.2014.4576.

Marouane, B., Klug, M., As, K.S., Engel, J., Reichel, S., Janneck, E., Peiffer, S., 2021. The potential of granulated schwertmannite adsorbents to remove oxyanions (SeO32−, SeO42−, MoO42−, PO43−, Sb(OH)6−) from contaminated water. J. Geochemical Explor. 223,. https://doi.org/10.1016/j.gexplo.2020.106708 106708.

Martín-Crespo, T., Gómez-Ortiz, D., Martín-Velázquez, S., 2019. Geoenvironmental Characterization of Sulfide Mine Tailings. In: Mazadiego, L.F., De Miguel Garcia, E., Barrio-Parra, F., Izquierdo-Díaz, M. (Eds.). Applied Geochemistry with Case Studies on Geological Formations, Exploration Techniques and Environmental Issues. IntechOpen. https://doi.org/10.5772/intechopen.84795.

Maurice, P.A., Hochella, M.F., 2008. Chapter 5 Nanoscale Particles and Processes. A New Dimension in Soil Science. Advances in Agronomy, first ed. Elsevier Inc. https://doi.org/10.1016/S0065-2113(08)00605-6.

Matrajt, G., Joswiak, D., Keller, L., Brownlee, D., 2002. Could Ferrihydrite be a Host Phase of Organics in IDPs? Meteorit. Planet. Sci. 37 (Supplement), A96.

McGILL, I.R., McENANEY, B., SMITH, D.C., 1976. Crystal structure of green rust formed by corrosion of cast iron. Nature 259 (5540), 200–201. https://doi.org/10.1038/259200a0.

Meng, X., Zhang, C., Zhuang, J., Zheng, G., Zhou, L., 2020. Assessment of schwertmannite, jarosite and goethite as adsorbents for efficient adsorption of phenanthrene in water and the regeneration of spent adsorbents by heterogeneous fenton-like reaction. Chemosphere 244, 125523. https://doi.org/10.1016/j.chemosphere.2019.125523.

Michel, F.M., Barron, V., Torrent, J., Morales, M.P., Serna, C.J., Boily, J.-F., Liu, Q., Ambrosini, A., Cismasu, A.C., Brown, G.E., 2010. Ordered ferrimagnetic form of ferrihydrite reveals links among structure, composition, and magnetism. Proc. Natl. Acad. Sci. 107 (7), 2787–2792. https://doi.org/10.1073/pnas.0910170107.

Michel, F.M., Ehm, L., Antao, S.M., Lee, P.L., Chupas, P.J., Liu, G., Strongin, D.R., Schoonen, M.A.A., Phillips, B.L., Parise, J.B., 2007. The Structure of Ferrihydrite, a Nanocrystalline Material. Science (80-. 316 (5832), 1726–1729. https://doi.org/10.1126/science:1142525.

Morris, R.V., Golden, D.C., Bell, J.F., Lauer, H.V., Adams, J.B., 1993. Pigmenting agents in martian soils: Inferences from spectral, Mössbauer, and magnetic properties of nanophase and other iron oxides in Hawaiian palagonitic soil PN-9. Geochim. Cosmochim. Acta 57 (19), 4597–4609.

Mullet, M., Guillemin, Y., Ruby, C., 2008. Oxidation and deprotonation of synthetic FeII–FeIII (oxy)hydroxycarbonate Green Rust: An X-ray photoelectron study. J. Solid State Chem. 181 (1), 81–89. https://doi.org/10.1016/j.jssc.2007.10.026.

Murad, E., 1988. The Mössbauer spectrum of "well"-crystallized ferrihydrite. J. Magn. Magn. Mater. 74 (2), 153–157. https://doi.org/10.1016/0304-8853(88)90062-5.

Murad, E., Taylor, R.M., 1984. The Mössbauer spectra of hydroxycarbonate green rust. Clay Miner. 19, 77–83. https://doi.org/10.1180/claymin.1984.019.1.08.

Muttik, N., McCubbin, F.M., Keller, L.P., Santos, A.R., McCutcheon, W.A., Provencio, P. P., Rahman, Z., Shearer, C.K., Boyce, J.W., Agee, C.B., 2014. Inventory of H2O in the ancient Martian regolith from Northwest Africa 7034: The important role of Fe oxides. Geophys. Res. Lett. 41, 8235–8244. https://doi.org/10.1002/2014GL062533.

Nakamura, K., Keller, L.P., Nakamura, T., Noguchi, T., Zoensky, M.E., 2004. Mineralogical study of hydrated IDPs: X-ray diffraction and transmission electron microscopy. In: Lunar and Planetary Science XXXV, pp. Abstract 1862.

Navrotsky, A., Mazeina, L., Majzlan, J., 2008. Size-Driven Structural and Thermodynamic Complexity in Iron Oxides. Science (80-. 319 (5870), 1635–1638. https://doi.org/10.1126/science:1148614.

Newman, S.P., Jones, W., 1998. Synthesis, characterization and applications of layered double hydroxides containing organic guests. New J. Chem. 22, 105–115. https://doi.org/10.1039/a708319j.

Nordstrom, D.K., Plummer, L.N., Langmuir, D., Busenberg, E., May, H.M., Jones, B.F., Parkhurst, D.L., 1990. Revised Chemical Equilibrium Data for Major Water–Mineral Reactions and Their Limitations, pp. 398–413. https://doi.org/10.1021/bk-1990-0416.ch031.

Norvell, W.A., Lindsay, W.L., 1982. Estimation of the concentra- tion of Fe3+ and the (Fe3+)(OH-)3 ion product from equilibria of EDTA in soil. Soil Sci. Soc. Am. J. 46 (4), 710–715.
Oliveira, M.L.S., Flores, E.M.M., Dotto, G.L., Neckel, A., Silva, L.F.O., 2021a. Nanomineralogy of mortars and ceramics from the Forum of Caesar and Nerva (Rome, Italy): The protagonist of black crusts produced on historic buildings. J. of Cleaner Production 278, 123982. https://doi.org/10.1016/j.jclepro.2020.123982.
Oliveira, M.L.S., Dotto, G.L., Pinto, D., Neckel, A., Silva, L.F.O., 2021b. Nanoparticles as vectors of other contaminants in estuarine suspended sediments: Natural and real conditions. Marine Pollut. Bullet. 168, 112429. https://doi.org/10.1016/j.marpolbul.2021.112429.
Ordonez, D., Valencia, A., Chang, N.-B., Wanielista, M.P., 2020. Synergistic effects of aluminum/iron oxides and clay minerals on nutrient removal and recovery in water filtration media. J. of Cleaner Production 275 (122728), 1–18.
Paikaray, S., Peiffer, S., 2012. Abiotic schwertmannite transformation kinetics and the role of sorbed As(III). Appl. Geochemistry 27, 590–597. https://doi.org/10.1016/j.apgeochem.2011.12.013.
Paredes, I., Otero, N., Soler, A., Green, A.J., Soto, D.X., 2020. Agricultural and urban delivered nitrate pollution input to Mediterranean temporary freshwaters. Agricult. Ecosyst. and Environ. 294, 1–12.
Peine, A., Tritschler, A., Küsel, K., Peiffer, S., 2000. Electron flow in an iron-rich acidic sediment—evidence for an acidity-driven iron cycle. Limnol. Oceanogr. 45, 1077–1087. https://doi.org/10.4319/lo.2000.45.5.1077.
Perez, J.P.H., Mangayayam, M.C., Rubio, S.N., Freeman, H.M., Tobler, D.J., Benning, L.G., 2018. Intercalation of aromatic sulfonates in 'green rust' via ion exchange. Energy Procedia 146, 179–187. https://doi.org/10.1016/j.egypro.2018.07.023.
H. Perez, J.P., Freeman, H.M., Brown, A.P., van Genuchten, C.M., Dideriksen, K., S'ari, M., Tobler, D.J., Benning, L.G., 2020. Direct visualization of arsenic binding on green rust sulfate. Environ. Sci. Technol. 54 (6), 3297–3305. https://doi.org/10.1021/acs.est.9b0709210.1021/acs.est.9b07092.s001.
Perez, J.P.H., Schiefler, A.A., Rubio, S.N., Reischer, M., Overheu, N.D., Benning, L.G., Tobler, D.J., 2021a. Arsenic removal from natural groundwater using 'green rust': Solid phase stability and contaminant fate. J. Hazard. Mater. 401, 123327. https://doi.org/10.1016/j.jhazmat.2020.123327.
Perez, J.P.H., Tobler, D.J., Freeman, H.M., Brown, A.P., Hondow, N.S., van Genuchten, C.M., Benning, L.G., 2021b. Arsenic species delay structural ordering during green rust sulfate crystallization from ferrihydrite. Environ. Sci.: Nano, Advanced Article. 8 (10), 2950–2963. https://doi.org/10.1039/D1EN00384D.
Pérez-López, R., Macías, F., Cánovas, C.R., Sarmiento, A.M., Pérez-Moreno, S.M., 2016. Pollutant flows from a phosphogypsum disposal area to an estuarine environment: An insight from geochemical signatures. Sci. of the Total EnviroN. 553, 42–51.
Polizzotto, M.L., Harvey, C.H., Li, G., Badruzzman, B., Ali, A., Newville, M., Sutton, S., Fendorf, S., 2006. Solid-phases and desorption processes of arsenic within Bangladesh sediments. Chem. Geol. 228 (1–3), 97–111. https://doi.org/10.1016/j.chemgeo.2005.11.026.
Posth, N.R., Kohler, I., Swanner, E.D., Schroder, C., Wellmann, E., Binder, B., Konhauser, K.O., Neumann, U., Berthold, C., Nowak, M., Kappler, A., 2013. Simulating Precambrian banded iron formation diagenesis. Chem. Geol. 362, 66–73. https://doi.org/10.1016/j.chemgeo.2013.05.031.
Poulton, S.W., Canfield, D.E., 2011. Ferruginous Conditions: A Dominant Feature of the Ocean through Earth's History. Elements 7 (2), 107–112. https://doi.org/10.2113/gselements.7.2.107.
Raiswell, R., Benning, L.G., Davidson, L., Tranter, M., Tulaczyk, S., 2009. Schwertmannite in wet, acid, and oxic microenvironments beneath polar and polythermal glaciers. Geology 37, 431–434. https://doi.org/10.1130/G25350A.1.
Raiswell, R., Canfield, D.E., 2012. The iron biogeochemical cycle past and present. Geochem. Persp. 1 (1), 1–232. https://doi.org/10.7185/geochempersp.1.1.
Raiswell, R., Hawkings, J.R., Benning, L.G., Baker, A.R., Death, R., Albani, S., Mahowald, N., Krom, M.D., Poulton, S.W., Wadham, J., Tranter, M., 2016. Potentially bioavailable iron delivery by iceberg-hosted sediments and atmospheric dust to the polar oceans. Biogeosciences 13 (13), 3887–3900. https://doi.org/10.5194/bg-13-3887-201610.5194/bg-13-3887-2016-supplement.
Rancourt, D.G., Meunier, J.-F., 2008. Constraints on structural models of ferrihydrite as a nanocrystalline material. Am. Mineral. 93, 1412–1417. https://doi.org/10.2138/am.2008.2782.
Refait, P.H., Abdelmoula, M., GÉnin, J.-M.-R., 1998a. Mechanisms of formation and structure of green rust one in aqueous corrosion of iron in the presence of chloride ions. Corros. Sci. 40 (9), 1547–1560. https://doi.org/10.1016/S0010-938X(98)00066-3.
Refait, P., Charton, A., Génin, J.-M.-R., 1998b. Identification, composition, thermodynamic and structural properties of a pyroaurite-like iron(II)-iron(III) hydroxy-oxalate Green Rust. Eur. J. Solid State Inorg. Chem. 35 (10-11), 655–666. https://doi.org/10.1016/S0992-4361(99)80006-X.
Refait, P., Simon, L., Génin, J.-M., 2000. Reduction of SeO42- anions and anoxic formation of iron(II)-iron(III) hydroxy selenate green rust. Environ. Sci. Technol. 34 (5), 819–825. https://doi.org/10.1021/es990376g.
Refait, P.h., Benali, O., Abdelmoula, M., Génin, J.-M.-R., 2003. Formation of 'ferric green rust' and/or ferrihydrite by fast oxidation of iron(II–III) hydroxychloride green rust. Corros. Sci. 45 (11), 2435–2449. https://doi.org/10.1016/S0010-938X(03)00073-8.
Refait, P., Abdelmoula, M., Génin, J.-M.R., Jeannin, M., 2007. Synthesis and characterisation of the Fe(II–III) hydroxy-formate green rust. In: ICAME 2005. Springer Berlin Heidelberg, pp. 717–722.
Regenspurg, S., Brand, A., Peiffer, S., 2004. Formation and stability of schwertmannite in acidic mining lakes. Geochim. Cosmochim. Acta 68, 1185–1197. https://doi.org/10.1016/j.gca.2003.07.015.
Root, R.A., Dixit, S., Campbell, K.M., Jew, A.D., Hering, J.G., O'Day, P.A., 2007. Arsenic sequestration by sorption processes in high-iron sediments. Geochim. Cosmochim. Acta 71 (23), 5782–5803. https://doi.org/10.1016/j.gca.2007.04.038.
Ruby, C., Géhin, A., Abdelmoula, M., Génin, J.-M., Jolivet, J.-P., 2003. Coprecipitation of Fe(II) and Fe(III) cations in sulphated aqueous medium and formation of hydroxysulphate green rust. Solid State Sci. 5 (7), 1055–1062. https://doi.org/10.1016/S1293-2558(03)00121-3.
Russell, J.D., 1979. Infrared spectroscopy of ferrihydrite: evidence for the presence of structural hydroxyl groups. Clay Miner. 14 (2), 109–114. https://doi.org/10.1180/claymin.1979.014.2.03.
Russell, M.J., 2018. Green Rust: The Simple Organizing 'Seed' of All Life? Life 8, 35. https://doi.org/10.3390/life8030035.
Sabot, R., Jeannin, M., Gadouleau, M., Guo, Q., Sicre, E., Refait, P.h., 2007. Influence of lactate ions on the formation of rust. Corros. Sci. 49 (3), 1610–1624. https://doi.org/10.1016/j.corsci.2006.10.004.
Sahoo, G., Fujieda, S., Shinoda, K., Yamaguchi, S., Korosaki, M., Suzuki, S., 2011. Influence of silicon species on the transformation of green rust I(Cl−) in aqueous solution by oxidation. Corros. Sci. 53 (12), 4001–4009. https://doi.org/10.1016/j.corsci.2011.08.003.
Sánchez-España, J., Yusta, I., Diez-Ercilla, M., 2011. Schwertmannite and hydrobasaluminite: A re-evaluation of their solubility and control on the iron and aluminium concentration in acidic pit lakes. Appl. Geochem. 26 (9-10), 1752–1774. https://doi.org/10.1016/j.apgeochem.2011.06.020.
Santos, M.S.F., Alves, A., Madeira, L.M., 2011. Paraquat removal from water by oxidation with Fenton's reagent. Chem. Eng. J. 175, 279–290.
Sanz, J.L., Rodríguez, N., Díaz, E.E., Amils, R., 2011. Methanogenesis in the sediments of Rio Tinto, an extreme acidic river. Environ. Microbiol. 13, 2336–2341. https://doi.org/10.1111/j.1462-2920.2011.02504.x.
Sassi, M., Rosso, K.M., 2019a. Roles of Hydration and Magnetism on the Structure of Ferrihydrite from First Principles. ACS Earth Sp. Chem. 3 (1), 70–78. https://doi.org/10.1021/acsearthspacechem.8b0013810.1021/acsearthspacechem.8b00138.s001.
Sassi, M., Rosso, K.M., 2019b. Reply to 'comment on Roles of Hydration and Magnetism on the Structure of Ferrihydrite from First Principles'. ACS Earth Sp. Chem. 3 (8), 1581–1583. https://doi.org/10.1021/acsearthspacechem.9b00160.
Schindler, P., Michaelis, W., Feitknecht, W., 1963. Löslichkeitsprodukte von Metalloxiden und -hydroxiden. 8. Mitteilung. Die Löslichkeit gealterter Eisen (III)-hydroxid-Fällungen. Helv. Chim. Acta 46, 444–449. https://doi.org/10.1002/hlca.19630460204.
Schneider, I.L., Teixeira, E.C., Dotto, G.L., Pinto, D., Yang, C.-X., Silva, L.F.O., 2020. Geochemical study of submicron particulate matter (PM1) in a metropolitan area. Geosci. Front., 101130 https://doi.org/10.1016/j.gsf.2020.12.011.
Schoepfer, V.A., Burton, E.D., Johnston, S.G., Kraal, P., 2019. Phosphate loading alters schwertmannite transformation rates and pathways during microbial reduction. Sci. Total Environ. 657, 770–780. https://doi.org/10.1016/j.scitotenv.2018.12.082.
Schoepfer, V.A., Burton, E.D., 2021. Schwertmannite: A review of its occurrence, formation, structure, stability and interactions with oxyanions. Earth-Sci. Rev. 221, 103811. https://doi.org/10.1016/j.earscirev.2021.103811.
Schroth, A.W., Parnell, R.A., 2005. Trace metal retention through the schwertmannite to goethite transformation as observed in a field setting, Alta Mine. MT. Appl. Geochem. 20 (5), 907–917. https://doi.org/10.1016/j.apgeochem.2004.09.020.
Schwertmann, U., Bigham, J.M., Murad, E., 1995. The first occurrence of schwertmannite in a natural stream environment. Eur. J. Mineral. 7 (3), 547–552. https://doi.org/10.1127/ejm/7/3/0547.
Schwertmann, U., Carlson, L., 2005. The pH-dependent transformation of schwertmannite to goethite at 25°C. Clay Miner. 40 (1), 63–66. https://doi.org/10.1180/0009855054010155.
Schwertmann, U., Fechter, H., 1994. The Formation of Green Rust and Its Transformation to Lepidocrocite. Clay Miner. 29 (1), 87–92. https://doi.org/10.1180/claymin.1994.029.1.10.
Schwertmann, U., Friedl, J., Stanjek, H., 1999. From Fe(III) ions to ferrihydrite and then to hematite. J. Colloid Interface Sci. 209 (1), 215–223. https://doi.org/10.1006/jcis.1998.5899.
Schwertmann, U., Friedl, J., Stanjek, H., Schulze, D.G., 2000. The effect of clay minerals on the formation of goethite and hematite from ferrihydrite after 16 years' ageing at 25°C and pH 4–7. Clay Miner. 35 (4), 613–623. https://doi.org/10.1180/000985500547034.
Schwertmann, U., Murad, E., 1983. Effect of pH on the Formation of Goethite and Hematite from Ferrihydrite. Clays Clay Miner. 31, 277–284. https://doi.org/10.1346/CCMN.1983.0310405.
Schwertmann, U., Stanjek, H., Becher, H.-H., 2004. Long-term in vitro transformation of 2-line ferrihydrite to goethite/hematite at 4, 10, 15 and 25°C. Clay Miner. 39 (4), 433–438. https://doi.org/10.1180/0009855043940145.
Sestu, M., Navarra, G., Carrero, S., Valvidares, S.M., Aquilanti, G., Pérez-Lopez, R., Fernandez-Martinez, A., 2017. Whole-nanoparticle atomistic modeling of the schwertmannite structure from total scattering data. J. Appl. Crystallogr. 50, 1617–1626. https://doi.org/10.1107/S160057671701336X.
Shannon, R.D., 1976. Revised effective ionic radii and systematic studies of interatomic distances in halides and chalcogenides. Acta Crystallogr. A 32 (5), 751–767. https://doi.org/10.1107/S0567739476001551.

Sharma, A., Ahmad, J., Flora, S.J.S., 2018. Application of advanced oxidation processes and toxicity assessment of transformation products. Environ. Res. 167, 223–233.
Shi, Z., Bonneville, S., Krom, M.D., Carslaw, K.S., Jickells, T.D., Baker, A.R., Benning, L. G., 2011. Iron dissolution kinetics of mineral dust at low pH during simulated atmospheric processing. Atmos. Chem. Phys. 11 (995–1007), 2011. https://doi.org/10.5194/acp-11-995-2011.
Shi, Z., Krom, M.D., Jickells, T.D., Bonneville, S., Carslaw, K.S., Mihalopoulos, N., Baker, A.R., Benning, L.G., 2012. Impacts on iron solubility in the mineral dust by processes in the source region and the atmosphere: A review. Aeolian Res. 5, 21–42. https://doi.org/10.1016/j.aeolia.2012.03.001.
Shi, M., Min, X., Ke, Y., Lin, Z., Yang, Z., Wang, S., Peng, N., Yan, X.u., Luo, S., Wu, J., Wei, Y., 2021. Recent progress in understanding the mechanism of heavy metals retention by iron (oxyhydr)oxides. Sci. of the Total Env. 752, 141930. https://doi.org/10.1016/j.scitotenv.2020.141930.
Shu, Z., Liu, L., Tan, W., Suib, S.L., Qiu, G., Yang, X., Zheng, L., Liu, F., 2019. Solar Irradiation Induced Transformation of Ferrihydrite in the Presence of Aqueous Fe2+. Environ. Sci. Technol. 53 (15), 8854–8861. https://doi.org/10.1021/acs.est.9b02750.
Sibrell, P.L., Kehler, T., 2016. Phosphorus removal from aquaculture effluents at the NortheastFishery Center in Lamar, Pennsylvania using iron oxide sorption media. Aquacultural Eng. 72-73, 45–52.
Sibrell, P.L., Montgomery, G.A., Ritenour, K.L., Tucker, T.W., 2009. Removal of phosphorus from agricultural wastewaters using adsorption media prepared from acid mine drainage sludge. Water Res. 43 (8), 2240–2250.
Silva, L.F.O., Lozano, L.P., Oliveira, M.L.S., da Boit, K., Gonçalves, J.O., Neckel, A., 2021a. Identification of hazardous nanoparticles present in the Caribbean Sea for the allocation of future preservation projects. Marine Pollut. Bullet. 168, 112425. https://doi.org/10.1016/j.marpolbul.2021.112425.
Silva, L.F.O., Pinto, D., Oliveira, M.L.S., Dotto, G.L., 2021b. Dispersion of hazardous nanoparticles on beaches around phosphogypsum factories. Marine Pollut. Bullet. 169, 112493. https://doi.org/10.1016/j.marpolbul.2021.112493.
Simon, L., Refait, P., Genin, J.M.R., 1998. Transformation of Fe(II)-Fe(III) hydroxysulphite into hydroxysulphate Green Rusts. Hyperfine Interact. 112, 217–220. https://doi.org/10.1023/A:1010845107110.
Simon, L., François, M., Refait, P., Renaudin, G., Lelaurain, M., Génin, J.-M., 2003. Structure of the Fe(II-III) layered double hydroxysulphate green rust two from Rietveld analysis. Solid State Sci. 5 (2), 327–334. https://doi.org/10.1016/S1293-2558(02)00019-5.
Singh, B., Gräfe, M., Kaur, N., Liese, A., 2010. Applications of synchrotron-based X-ray diffraction and X-ray absorption spectroscopy to the understanding of poorly crystalline and metal-substituted Iron oxides. Dev. Soil Sci. 34, 199–254. https://doi.org/10.1016/s0166-2481(10)34008-6.
Slomp, C.P., Van der Gaast, S.J., Van Raaphorst, W., 1996. Phosphorus binding by poorly crystalline iron oxides in North Sea sediments. Marine Chem. 52 (1), 55–73. https://doi.org/10.1016/0304-4203(95)00078-X.
Smetacek, V., Klaas, C., Strass, V.H., Assmy, P., Montresor, M., Cisewski, B., Savoye, N., Webb, A., d'Ovidio, F., Arrieta, J.M., Bathmann, U., Bellerby, R., Berg, G.M., Croot, P., Gonzalez, S., Henjes, J., Herndl, G.J., Hoffmann, L.J., Leach, H., Losch, M., Mills, M.M., Neill, C., Peeken, I., Röttgers, R., Sachs, O., Sauter, E., Schmidt, M.M., Schwarz, J., Terbrüggen, A., Wolf-Gladrow, D., 2012. Deep carbon export from a Southern Ocean iron-fertilized diatom bloom. Nature 487 (7407), 313–319.
Smuda, J., Dold, B., Friese, K., Morgenstern, P., Glaesser, W., 2007. Mineralogical and geochemical study of element mobility at the sulfide-rich Excelsior waste rock dump from the polymetallic Zn–Pb–(Ag–Bi–Cu) deposit, Cerro de Pasco. Peru. J. of Geoch. Explor. 92 (2-3), 97–110. https://doi.org/10.1016/j.gexplo.2006.08.001.
Stampfl, P.P., 1969. Ein basisches eisen-II-III-karbonat in rost. Corros. Sci. 9 (3), 185–187. https://doi.org/10.1016/S0010-938X(69)80029-6.
Stanjek, H., Weidler, P.G., 1992. The effect of dry heating on the chemistry, surface area, and oxalate solubility of synthetic 2-line and 6-line ferrihydrites. Clay Miner. 27 (4), 397–411.
Stefánsson, A., 2007. Iron (III) hydrolysis and solubility at 25 degrees C. Environ. Sci. Technol. 41, 6117–61123.
Suzuki, S., Matsubara, E., Komatsu, T., Okamoto, Y., Kanie, K., Muramatsu, A., Konishi, H., Mizuki, J., Waseda, Y., 2007. Ex-situ and in-situ X-ray diffractions of corrosion products freshly formed on the surface of an iron-silicon alloy. Corros. Sci. 49 (3), 1081–1096. https://doi.org/10.1016/j.corsci.2006.06.029.
Takahashi, Y., Furukawa, T., Kanai, Y., Uematsu, M., Zheng, G., Marcus, M.A., 2013. Seasonal changes in Fe species and soluble Fe concentration in the atmosphere in the Northwest Pacific region based on the analysis of aerosols collected in Tsukuba. Japan. Atmos. Chem. Phys. 13 (15), 7695–7710. https://doi.org/10.5194/acp-13-7695-201310.5194/acp-13-7695-2013-supplement.
Takahashi, Y., Matsubara, E., Suzuki, S., Okamoto, Y., Komatsu, T., Konishi, H., Mizuki, J., Waseda, Y., 2005. In-situ X-ray diffraction of corrosion products formed on iron surfaces. Mater. Trans. 46, 637–642. https://doi.org/10.2320/matertrans.46.637.
Taylor, R.M., 1980. Formation and properties of Fe (II)Fe(III) hydroxy-carbonate and its possible significance in soil formation. Clay Miner. 15 (4), 369–382. https://doi.org/10.1180/claymin.1980.015.4.04.
ThomasArrigo, L.K., Kaegi, R., Kretzschmar, R., 2019. Ferrihydrite Growth and Transformation in the Presence of Ferrous Iron and Model Organic Ligands. Environ. Sci. Technol. 53 (23), 13636–13647. https://doi.org/10.1021/acs.est.9b0395210.1021/acs.est.9b03952.s001.
Tomeoka, K., Buseck, P.R., 1988. Matrix mineralogy of the Orgueil CI carbonaceous chondrite. Geochim. Cosmochim. Acta 52 (6), 1627–1640. https://doi.org/10.1016/0016-7037(88)90231-1.
Tosca, N.J., Knoll, A.H., McLennan, S.M., 2008. Water activity and the challenge for life on early mars. Science 320 (5880), 1204–1207.
Towe, K.M., Bradley, W.F., 1967. Mineralogical constitution of colloidal "hydrous ferric oxides". J. Colloid Interface Sci. 24, 384–392. https://doi.org/10.1016/0021-9797(67)90266-4.
Treiman, A.H., Morris, R.V., Agresti, D.G., Graff, T.G., Achilles, C.N., Rampe, E.B., Bristow, T.F., Blake, D.F., Vaniman, D.T., Bish, D.L., Chipera, S.J.S.J., Morrison, S.M. M.S.M., Downs, R.T.R.T., 2014. Curiosity at Gale Crater, Mars: Characterization and Analysis of the Rocknest Sand Shadow. Science 80). 341, 7071–7076.
Trejos, E.M., Silva, L.F.O., Hower, J.C., Flores, E.M.M., González, C.M., Pachón, J.E., Aristizábal, B.H., 2021. Volcanic emissions and atmospheric pollution: A study of nanoparticles. Geosci. Front. 12 (2), 746–755.
Trolard, F., Génin, J.-M.-R., Abdelmoula, M., Bourrié, G., Humbert, B., Herbillon, A., 1997. Identification of a green rust mineral in a reductomorphic soil by Mossbauer and Raman spectroscopies. Geochim. Cosmochim. Acta 61 (5), 1107–1111. https://doi.org/10.1016/S0016-7037(96)00381-X.
Trolard, F., Bourrié, G., Abdelmoula, M., Refait, P., Feder, F., 2007. Fougerite, a new mineral of the pyroaurite-iowaite group: Description and crystal structure. Clays Clay. Miner. 55 (3), 323–334. https://doi.org/10.1346/CCMN.2007.0550308.
Truesdell, A.H., Jones, B.F., 1974. WATEQ, a computer program for calculating chemical equilibria of natural waters. J. Res. U. S. Geol. Surv. 2, 233–246.
Urbonas, B., Stahre, P., 1993. Stormwater: Best Management Practices and Detention for Water Quality, Drainage, and CSO Management. PTR Prentice Hall, pp. 471.
Usman, M., Byrne, J.M., Chaudhary, A., Orsetti, S., Hanna, K., Ruby, C., Kappler, A., Haderlein, S.B., 2018. Magnetite and green rust: Synthesis, properties, and environmental applications of mixed-valent iron minerals. Chem. Rev. 118 (7), 3251–3304.
van Genuchten, C.M., Behrends, T., Dideriksen, K., 2019. Emerging investigator series: Interdependency of green rust transformation and the partitioning and binding mode of arsenic. Environ. Sci. Process Impacts 21 (9), 1459–1476. https://doi.org/10.1039/C9EM00267G.
Vaughan, G., Brydson, R., Brown, A., 2012. Characterisation of Synthetic Two-line Ferrihydrite by Electron Energy Loss Spectroscopy. J. Phys. Conf. Ser. 371, 12079. https://doi.org/10.1088/1742-6596/371/1/012079.
Vaziri Hassas, B., Rezaee, M., Pisupati, S.V., 2020. Precipitation of rare earth elements from acid mine drainage by CO2 mineralization process. Chem. Eng. J. 399, 125716. https://doi.org/10.1016/j.cej.2020.125716.
Vinš, J., Šubrt, J., Zapletal, V., Hanousek, F., 1987. Preparation and properties of green rust type substances. Collect. Czech. Chem. Commun. 52 (1), 93–102. https://doi.org/10.1135/cccc19870093.
Vithana, C.L., Sullivan, L.A., Burton, E.D., Bush, R.T., 2015. Stability of schwertmannite and jarosite in an acidic landscape: Prolonged field incubation. Geoderma 239, 47–57. https://doi.org/10.1016/j.geoderma.2014.09.022.
Vodyanitskii, Y.N., Shoba, S.A., 2016. Ferrihydrite in soils. Eurasian Soil Sci. 49 (7), 796–806. https://doi.org/10.1134/S1064229316070127.
von der Heyden, B.P., Roychoudhury, A.N., Mtshali, T.N., Tyliszczakand, T., Myneni, S.C.B., 2012. Chemically and Geographically Distinct Solid-Phase Iron Pools in the Southern Ocean. Science 338 (6111), 1199–1201. https://doi.org/10.1126/science.1227504.
Vu, H.P., Shaw, S., Benning, L.G., 2008. Transformation of ferrihydrite to hematite: an in situ investigation on the kinetics and mechanisms. Mineral. Mag. 72 (1), 217–220. https://doi.org/10.1180/minmag.2008.072.1.217.
Vuillemin, A., Wirth, R., Kemnitz, H., Schleicher, A.M., Friese, A., Bauer, K.W., Simister, R., Nomosatryo, S., Ordonez, L., Ariztegui, D., Henny, C., Crowe, S.A., Benning, L.G., Kallmeyer, J., Russell, J.M., Bijaksana, S., Vogel, H., Team, T.D.P.S., 2019. Formation of diagenetic siderite in modern ferruginous sediments. Geology 47, 540–544. https://doi.org/10.1130/G46100.1.
Wang, X., Liu, F., Tan, W., Feng, X., Koopal, L.K., 2013. Transformation of hydroxycarbonate green rust into crystalline iron (hydr)oxides: Influences of reaction conditions and underlying mechanisms. Chem. Geol. 351, 57–65. https://doi.org/10.1016/j.chemgeo.2013.05.003.
Wang, Y., Morin, G., Ona-Nguema, G., Brown, G.E., 2014. Arsenic(III) and arsenic(V) speciation during transformation of lepidocrocite to magnetite. Environ. Sci. Technol. 48 (24), 14282–14290. https://doi.org/10.1021/es5033629.
Wang, X., Peng, J., Liang, X., Zhu, M., Lanson, B., Wang, L., Liang, X., Liu, F., Tan, W., Feng, X., 2019. Effects of Mn2+, Ni2+, and Cu2+ on the Formation and Transformation of Hydrosulfate Green Rust: Reaction Processes and Underlying Mechanisms. ACS Earth Space Chem. 3 (4), 519–530. https://doi.org/10.1021/acsearthspacechem.8b0018710.1021/acsearthspacechem.8b00187.s001.
Waychunas, G.A., Rea, B.A., Fuller, C.C., Davis, J.A., 1993. Surface chemistry of ferrihydrite: Part 1. EXAFS studies of the geometry of coprecipitated and adsorbed arsenate. Geochim. Cosmochim. Acta 57 (10), 2251–2269. https://doi.org/10.1016/0016-7037(93)90567-G.
Waychunas, G.A., Xu, N., Fuller, C.C., Davis, J.A., Bigham, J.M., 1995. XAS study of AsO43− and SeO42− substituted schwertmannites. Phys. B Condens. Matter 208–209, 481–483. https://doi.org/10.1016/0921-4526(94)00730-J.
Wei, X., Viadero, R.C., Bhojappa, S., 2008. Phosphorus removal by acid mine drainage sludge from secondary effluents of municipal wastewater treatment plants. Water Reserch 42 (13), 3275–3284.
Wen, D., Chang, N.B., Wanielista, M.P., 2020. Assessing Nutrient Removal in Stormwater Runoff for Urban Farming with Iron filings-based Green Environmental Media. Sci. Rep. 10 (9379), 1–13.

West, L., McGown, D.J., Onstott, T.C., Morris, R.V., Suchecki, P., Pratt, L.M., 2009. High Lake gossan deposit: an Arctic analogue for ancient Martian surficial processes? Planetary and Space Sci. 57 (11), 1302–1311.

Xu, W., Hausner, D.B., Harrington, R., Lee, P.L., Strongin, D.R., Parise, J.B., 2011. Structural water in ferrihydrite and constraints this provides on possible structure models. Am. Mineral. 96 (4), 513–520. https://doi.org/10.2138/am.2011.3460.

Yan, L., Zhu, R., Liu, J., Yang, Y., Zhu, J., Sun, H., He, H., 2020. Effects of Fullerol and Graphene Oxide on the Phase Transformation of Two-Line Ferrihydrite. ACS Earth Sp. Chem. 4 (3), 335–344. https://doi.org/10.1021/acsearthspacechem.9b0026110.1021/acsearthspacechem.9b00261.s001.

Yang, G.C.C., 2019. Integrated electrokinetic processes for the remediation of phthalate esters in river sediments: A mini-review. Sci. of the Tot. Env. 659, 963–972.

Yee, N., Shaw, S., Benning, L.G., Nguyen, T.H., 2006. The rate of ferrihydrite transformation to goethite via the Fe(II) pathway. Am. Mineral. 91 (1), 92–96. https://doi.org/10.2138/am.2006.1860.

Yousefi, Z., Ala, A., Babanezhad, E., Ali Mohammadpour, R., 2019. Evaluation of exposure to phthalate esters through the use of various brands of drinking water bottled in polyethylene terephthalate (PET) containers under different storage conditions. Environ. Health Eng. Manag. 6 (4), 247–255.

Younger, P.L., Banwart, S., Hedin, R.S., 2002. Mine Water: Hydrology, Pollution, Remediation. Kluwer Academic Publisher London, UK, pp. 442.

Yu, J.-Y., Heo, B., Choi, I.-K., Cho, J.-P., Chang, H.-W., 1999. Apparent solubilities of schwertmannite and ferrihydrite in natural stream waters polluted by mine drainage. Geochim. Cosmochim. Acta 63 (19-20), 3407–3416. https://doi.org/10.1016/S0016-7037(99)00261-6.

Yu, J.-Y., Park, M., Kim, J., 2002. Solubilities of synthetic schwertmannite and ferrihydrite. Geochem. J. 36 (2), 119–132. https://doi.org/10.2343/geochemj.36.119.

Yutaka, T., Takashi, Y., Takashi, K., 1984. The Synthesis of Green Rust II(FeIII1–FeII2) and Its Spontaneous Transformation into Fe3O4. Bull. Chem. Soc. Japan 57, 2411–2416. https://doi.org/10.1246/bcsj.57.2411.

Zegeye, A., Bonneville, S., Benning, L.G., Sturm, A., Fowle, D.A., Jones, C., Canfield, D. E., Ruby, C., MacLean, L.C., Nomosatryo, S., Crowe, S.A., Poulton, S.W., 2012. Green rust formation controls nutrient availability in a ferruginous water column. Geology 40, 599–602. https://doi.org/10.1130/G32959.1.

Zhang, Z., Bi, X., Li, X., Zhao, Q., Chen, H., 2018a. Schwertmannite: occurrence, properties, synthesis and application in environmental remediation. RSC Adv. 8 (59), 33583–33599. https://doi.org/10.1039/C8RA06025H.

Zhang, M.-H., Dong, H., Zhao, L., Wang, D.-x., Meng, D.i., 2019. A review on Fenton process for organic wastewater treatment based on optimization perspective. Sci. Total Environ. 670, 110–121.

Zhang, P., Huang, W., Ji, Z., Zhou, C., Yuan, S., 2018b. Mechanisms of hydroxyl radicals production from pyrite oxidation by hydrogen peroxide: Surface versus aqueous reactions. Geochim. Cosmochim. Acta 238, 394–410.

Zhang, D., Wang, S., Wang, Y., Gomez, M.A., Duan, Y., Jia, Y., 2018c. The Transformation of Two-Line Ferrihydrite into Crystalline Products: Effect of pH and Media (Sulfate versus Nitrate). ACS Earth Sp. Chem. 2 (6), 577–587. https://doi.org/10.1021/acsearthspacechem.8b0000110.1021/acsearthspacechem.8b00001.s001.

Zhao, J., Huggins, F.E., Feng, Z., Huffman, G.P., 1994. Ferrihydrite: Surface Structure and Its Effects on Phase Transformation. Clays Clay Miner. 42, 737–746. https://doi.org/10.1346/CCMN.1994.0420610.